HAL
open science

Growth and study of Tb^{3+} doped Nb_2O_5 thin films by radiofrequency magnetron sputtering: photoluminescence properties

Bryan Horcholle, Christophe Labbé, Xavier Portier, Philippe Marie, Cédric Frilay, Weiqiang Yuan, Wojciech Jadwisienczak, David Ingram, Clara Grygiel, Julien Cardin

To cite this version:

Bryan Horcholle, Christophe Labbé, Xavier Portier, Philippe Marie, Cédric Frilay, et al.. Growth and study of Tb^{3+} doped Nb_2O_5 thin films by radiofrequency magnetron sputtering: photoluminescence properties. Applied Surface Science, 2022, 597, pp.153711. 10.1016/j.apsusc.2022.153711 . hal-03675408

HAL Id: hal-03675408

https://hal.science/hal-03675408

Submitted on 21 Sep 2023

HAL is a multi-disciplinary open access archive for the deposit and dissemination of scientific research documents, whether they are published or not. The documents may come from teaching and research institutions in France or abroad, or from public or private research centers.

L'archive ouverte pluridisciplinaire **HAL**, est destinée au dépôt et à la diffusion de documents scientifiques de niveau recherche, publiés ou non, émanant des établissements d'enseignement et de recherche français ou étrangers, des laboratoires publics ou privés.

Growth and study of Tb^{3+} doped Nb_2O_5 thin films by radiofrequency magnetron sputtering: Photoluminescence properties

Bryan Horcholle [a], Christophe Labbé [a], Xavier Portier [a], Philippe Marie [a], Cédric Frilay [a], Weiqiang Yuan [b], Wojciech Jadwisienczak [b], David Ingram [c], Clara Grygiel [a], Julien Cardin [a,*]

[a] CIMAP, Normandie Université, ENSICAEN, UNICAEN, CEA, CNRS, 6 Boulevard Maréchal Juin 14050 Caen Cedex 4, France
[b] School of Electrical Engineering and Computer Science, Ohio University, Athens, OH 45701, USA
[c] Department of Physics and Astronomy, Ohio University, Athens, OH 45701, USA

Keywords:
Niobium
Rare Earth Doping
Terbium
Magnetron Sputtering
Luminescence
Optical Materials

A B S T R A C T

Undoped and doped Nb_2O_5 thin films were successfully deposited on silicon wafer by sputtering technique from high purity Nb_2O_5 and Tb_4O_7 targets and annealed by rapid thermal annealing between 400 °C and 900 °C. Chemical and structural investigations of undoped and Tb-doped Nb_2O_5 films were made, leading to the determination of stoichiometry and identification of phase transformations with increasing annealing temperature and Tb^{3+} ion content. The optical properties' analysis (spectrophotometry UV–Vis-NIR, spectroscopic ellipsometry) of those undoped and doped Nb_2O_5 films led us to the determination of refractive index and electronic properties evolution with annealing temperature and Tb^{3+} ion content. The structural evolution was confirmed by analysis of Raman spectra of undoped and doped Nb_2O_5 films. The photoluminescence properties of Tb^{3+} ion-doped Nb_2O_5 thin films were also studied. The correlation between the photoluminescence of Tb^{3+} ion and the electronic properties of the Nb_2O_5 host matrix is highlighted. The relationship between the structural modifications, the electronic properties of the host matrix, and the photoluminescence of Tb^{3+} ion is established.

1. Introduction

Niobium pentoxide films find many applications in several modern technologies due to their interesting properties. They are considered as corrosion-resistant materials[1], waveguides constituent materials for second harmonic optical generation[2], oxygen-sensitive materials for sensors[3], electrochromic materials[4,5], and catalytic material[6]. Due to their high refractive index n and low extinction coefficient k values in the visible range, Nb_2O_5 thin films are more particularly interesting for many optical functionalities as a building block of optical waveguides[2] with linear and non-linear properties. Moreover, in the low k spectral range, high n materials are attractive for building alternation with low n materials leading to high refractive index contrast, which is crucial for realizing interference optical filters[7].

Niobium pentoxide thin films are produced in different manners. They can be grown by chemical processes such as chemical vapor deposition[8], Atomic Layer Deposition (ALD)[9], or sol–gel method [10]. Moreover, they can be produced by physical processes such for instance by plasma electrolytic oxidation[11], or by Physical Vapor Deposition (PVD). Among PVD techniques, the magnetron radio-frequency sputtering[12] method allows growing homogenous thin films and to tune the incorporation of elements including rare earth (RE) elements in the pentoxide niobium host matrix by co-sputtering[13].

Rare earth-based phosphors are used in a wide range of applications such as in fluorescent lamps[14], biochemical sensors[15], X-ray intensifying screens[16], and down-converting layers[17,18]. In the literature, some studies can be found on Nb_2O_5 doped with other RE^{3+} ions (Eu^{3+}, La^{3+}, Sm^{3+}, Er^{3+})[11,19–21]. Those studies showed efficient RE^{3+} ions photoluminescence originating from 4f to 4f transitions in those doped Nb_2O_5 host matrices. To our knowledge, no studies have been realized on terbium (Tb) doping of the Nb_2O_5 host matrix. The Tb^{3+} ion is known to produce green emissions originating from radiative recombination from $^5D_4$ to $^iF_6$ with i = 1, 2, 3,…7 energy levels within 4f energy levels[22].

Few works in the literature reported Nb_2O_5 depositions with the sputtering technique[13]. In this study, we investigate undoped and Tb^{3+} doped Nb_2O_5 thin films grown by radio frequency magnetron sputtering technique and subsequent Rapid Thermal Annealing (RTA).

This work aims to explore the growth conditions by sputtering and rapid annealing of undoped and Tb-doped Nb_2O_5 films, subsequently. Combined structural and optical properties studies of the same undoped and doped matrix allow us to understand the mechanisms of light absorption and optical emission in the Nb_2O_5 host matrix.

The use of well-understood RE ions as a phosphor offers the advantage of its stable emission properties due to the optically active *4f* electrons masked by the outer 5 s2-5p6 electron shell. Hence, in this work, different undoped and Tb-doped Nb_2O_5 samples deposited by magnetron sputtering technique have been grown with various Tb^{3+} ion contents and post-deposition annealing temperatures. Structural properties were investigated using Rutherford Backscattering Spectroscopy (RBS), X-Ray Diffraction (XRD), and Transmission Electron microscopy (TEM) in High-resolution mode (HRTEM), scanning mode with High Angle annular dark-field (STEM HAADF). The optical and luminescent properties were examined using several techniques (ellipsometry, optical transmission, Raman, photoluminescence spectroscopy) and related to the structural properties.

2. Material and methods

Undoped Nb_2O_5 films were prepared by magnetron radiofrequency sputtering on (1 0 0) oriented P doped double faces polished Si substrate. A two-inch diameter 99.95% pure Nb_2O_5 target was used in pure argon (Ar) atmosphere under a flow of 10 sccm. The power density (P_{Nb2O5}) on the Nb_2O_5 target was 4.44 $W.cm^{-2}$. In addition, the pressure during the deposition was stabilized at 0.4 Pa (3mTorr) for 1 h and the deposition temperature of the substrate was fixed to 200 °C, respectively. Tb-doped Nb_2O_5 films were prepared in a similar way as undoped Nb_2O_5 by simultaneous magnetron radiofrequency co-sputtering of Nb_2O_5 and Tb_4O_7 99.95% pure two-inch diameter target. To adjust the doping rate, the power density (PD_{Tb4O7}) on the Tb_4O_7 target was varied by adjusting to the following six values 1.78, 2.07, 2.37, 2.66, 2.96, and 3.26 $W.cm^{-2}$, respectively. After deposition on the wafers, these were cut into 1 cm × 1 cm samples, which were annealed in the AS-One RTA system from Annealsys Company. The RTA is characterized by a temperature rise with a ramp of 20 °C.s^{-1} up to a stable temperature setpoint which was held for 4 min under an argon atmosphere at 1013 hPa. The temperature setpoint (T_A) ranges from 400 °C to 900 °C with 100 °C steps. Subsequently, the samples were cooled down to room temperature using water circulation in 180 s. All the Tb-doped samples were annealed with similar post-deposition annealing conditions.

The layer compositions were determined by RBS at the Edwards Accelerator Laboratory of Ohio University[24] using a 4.5MV tandem accelerator. To avoid channeling of the substrate by the analysis beam, the samples were oriented at an angle of 7.5° with respect to the incoming ion beam and placed on the sample holder so that no major plane was within 20° to the vertical or horizontal. The samples were irradiated with a 2.2 MeV $^4He^{++}$ ion beam. The energy resolution obtained on the sample was 20–30 keV, depending on the depth at which the analysis was performed. The elemental concentration was obtained by fitting the data with RUMP simulation software[25] with an accuracy of 2 % for Nb, 7.6 % for O, and 8 % for Tb with 2% of systematic error.

X-ray diffraction experiments were performed with a Bruker D8 Discover equipment using a parallel beam geometry with a Göbel mirror for K_α copper radiation source ($\lambda = 1.5418$ Å). The diffractometer has an Euler cradle allowing various movements where sample and detector are rotated. The diffraction angle between the incident beam and the detector is 2θ, while ω is the angle of incidence between the X-ray source and the sample surface. The recorded scans use symmetric geometry with $2\theta = 2\omega$ conditions. All measurements were carried out using the same optics settings (e.i. 1.2 mm slits, Soller slits of 2.5°, 1D LYNXEYE XE detector) in the 2θ range 10-100° by 0.0118° and 0.5 s per step, respectively. DIFFRAC. EVA Brucker software was used to determine the peak positions with the full width at half maximum (FWHM) of the selected XRD peak and to calculate the interplanar spacing d_{hkl} that led to the determination of phases.

Transmission Electronic Microscopy observations were performed with a double corrected (probe and imaging) JEOL ARM200F microscope equipped with a cold FEG (Field Emission Gun) source operated at 200 kV. The point-to-point resolution was about 1.0 Å in high-resolution mode (HRTEM). This microscope was also implemented with a scanning system (STEM) which offered the possibility to generate chemical contrast images (resolution of 0.78 Å) owing to a high angle annular dark-field (HAADF) detector as well as STEM EDX chemical mapping at a nanometer scale owing to a CENTURIO JEOL EDX spectrometer. The chemical maps were obtained from scans using 5 ms acquisition time, about 1000 counts per second accumulation with a dead-time of about 2%, respectively. The thin foils for electron transparency were prepared with a focused ion beam (FIB) system (FEI HELIOS NanoLab 660). Before the thinning procedure, to protect the film surfaces from the gallium beam, a thin carbon film (a few tens of nm thick) was deposited on the top of the sample film. Afterward, a platinum film (a few microns thick) was deposited to protect the whole film from the gallium beam during the thinning process. The carbon film allowed the top of the film to be discriminated from the bottom of the platinum protection during TEM observations.

The optical reflectance of samples was measured using a Perkin Elmer 1050 Lambda UV–Vis-NIR dual-beam spectrophotometer with a Universal Reflectance Accessory (URA). This URA allows performing absolute specular reflectance measurement at an angle ranging from 8° to 65°. The samples were measured at an angle of incidence of 8° by an incoming wave polarized in TE mode and with an optical beam of square shape and size of 5x5 mm^2. A transfer-matrices method-based program was created to calculate the TE and TM polarized reflectance, transmittance, and absorbance of a stack of layers comprise between a superstrate of air and a substrate. Nb_2O_5 material dispersion formula used is described by the Tauc-Lorentz (TL) model, which is suitable for describing amorphous semiconductors and insulators. The agreement between the measurement and the fit was determined with a Chi-squared like function.

$$\chi^2_{URA} = \frac{1}{N}\sum_{\lambda_{min}}^{\lambda_{max}}\left(\frac{R_{cal}(\lambda) - R_{mes}(\lambda)}{Tol}\right)^2 \quad (1)$$

where N was the number of points, $R_{cal}(\lambda)$ and $R_{mes}(\lambda)$ are respectively the calculated and measured reflectance at one wavelength λ, *Tol* is a tolerance factor that has the dimension of a variance chosen equal to 0.01 during calculation.

This dispersion model uses several parameters of physical interest which are the bandgap energy E_g, the oscillator's strength A_i, the energy position E_i of absorption/extinction coefficient peak, and the broadening term C_i. Depending on the kind of samples, single or double oscillators TL models were used to better describe the dielectric property of investigated material. The known materials as from superstrate or substrate are described by either direct refractive indexes file or by suitable particular dielectric model. Adopting an adapted modeling and fitting program based on the transfer matrix method and the Genetic algorithm method[26] the unknown film thickness, rough layer, and dielectric function parameters were obtained by fitting experimental reflectance obtained by Universal Reflectance Accessory (URA) measurement. Experimental uncertainties were obtained by a Monte Carlo re-sampling technique[26] based on uncertainties obtained from measurements.

The thickness and complex refractive index of samples were determined using Horiba Jobin-Yvon UVISEL Variable Angle Spectroscopic Ellipsometer (VASE) method. The experimental ellipsometer function I_c and I_s, deriving from classical function Δ and ψ, were recorded with multi-angle of incidence of 65°, 70°, 75° and in an energy range of 1.5 to 6 eV with 0.01 eV energy step. A structural and dielectric model was built in the deltapsi2 software[27] comprising a semi-infinite substrate surmounted by a homogeneous layer of the studied material and

surmounted by a layer of materials having an effective refractive index described by the Bruggeman effective medium (EM) model describing the layer surface roughness formed by a certain ratio of the studied material and void of air. The studied material's film thickness and complex refractive index were determined by fitting experimental data I_c and I_s using DeltaPsi2 software. All samples were measured with a spectroscopic ellipsometer before and after annealing. Similarly, as in reflectance, a TL dielectric model[28–30] was chosen for studying all the samples according to the previous description of Nb_2O_5 refractive index n and extinction coefficient k, respectively [31], and to its Kramers-Kronig consistency. A double oscillator TL model with height parameters was used for unannealed samples while a single oscillator TL model with five parameters was used for annealed samples. Experimental uncertainties were obtained by a Monte Carlo re-sampling technique based on TL models parameters uncertainties obtained by prior fitting with Horiba software.

Raman measurements were performed using the *Bruker SENTERRA* Raman microscope equipped with 1200 grooves/mm grating, thermoelectrically cooled *Andor IDus DU420 CCD* detector, and the *Bruker OPUS* software. The spectral resolution of the Raman system was better than 3 cm^{-1}. The 50X objective was used for all Raman spectra collections. The films were excited with a 532 nm green laser with 20 mW optical power. The Raman spectra were collected in the 190 cm^{-1} to 1100 cm^{-1}spectral range with an exposure time of 40 s and 5 times averaging to reduce the noise. The Raman spectra background correction was performed for Nb_2O_5 and Tb-doped Nb_2O_5 films measured to eliminate signal from Si substrate. Also, the Raman spectra evolution due to use the Tb_4O_7 target sputtering power and post-growth thermal annealing effects were carried out for all samples by performing the Raman spectra deconvolution and fitting procedures to determine the peak position and FWHM of selected Raman spectra using the *Originlab Pro* software.

To investigate the absorption, excitation, and emission mechanisms, PL measurements were realized at room temperature. The PL set-up used a Crylas CW FQCW-266–25 laser as an excitation source at 266 nm wavelength with a power density of 3 $W.cm^{-2}$. The PL signal is collected and dispersed through a Horiba Jobin-Yvon TRIAX180 monochromator. At the monochromator exit, the emission is detected using a Hamamatsu (R5108) PM tube and the detector signal is amplified by a FEMTO DLPCA-200 *trans*-impedance amplifier. The signal is recorded by a DSP SR830 lock-in amplifier referenced at the excitation light chopped frequency and driven using a homemade LabVIEW program controlled by PC.

3. Results

In this work, undoped Nb_2O_5 films and Tb-doped Nb_2O_5 were prepared on Si substrate according to the method described previously in the experimental section. First, undoped samples were produced with a variation of post-deposition annealing conditions. Secondly, Tb doped samples were made with a variation of the rare earth concentrations and similarly to undoped samples post-deposition, annealed with the same conditions as undoped samples. Different Tb doping rates tuned by the variation of power density (PD_{Tb4O7}) were investigated. First, *we present hereafter the combined analysis of the composition and microstructure of non-doped and doped Nb_2O_5 films by RBS, XRD, and TEM followed by the study of optical properties by ellipsometry, spectrophotometry, and Raman spectroscopy as a function of the sputtering and annealing parameters. In the last step, we will present the PL spectroscopy of the Tb doped Nb_2O_5 films according to the method described in the experimental method.*

3.1. Structural studies

To characterize the film's composition, RBS measurements were conducted for selected two undoped samples, one unannealed and the other annealed at 800 °C. The RBS spectra show Nb and O peaks heights

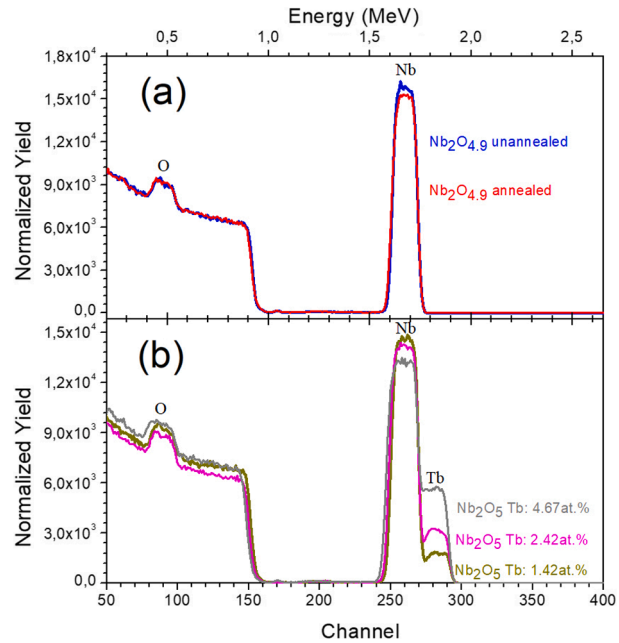

Fig. 1. RBS spectra of Nb_2O_5 samples (a) undoped unannealed and annealed at 800 °C (b) doped with various PD_{Tb4O7} of 1.78, 2.07, and 2.66 $W.cm^{-2}$ and annealed at 800 °C, respectively.

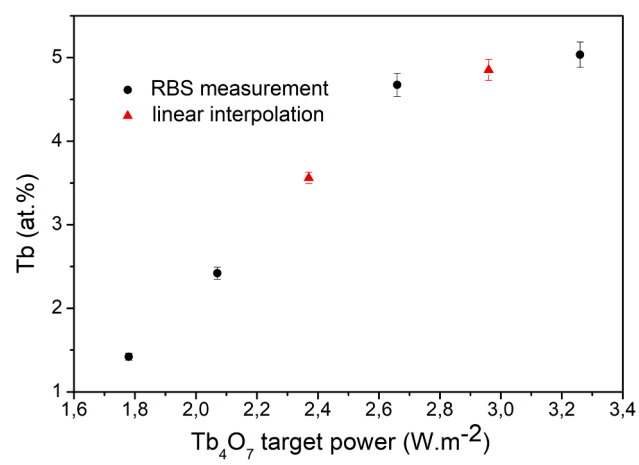

Fig. 2. Terbium atomic concentration in at.% as a function of the power density on the Tb_4O_7 target. The two red points were determined by linear interpolation.

and widths that remain identical before and after annealing, confirming the stability of the film stoichiometry with annealing treatment. Element contents present in the films were estimated by fitting the RBS profile shown in Fig. 1(a). Peaks attributed to Nb and O are similar for the unannealed and annealed samples. The determination of the stoichiometry for these two samples by RBS leads to the same stoichiometry of $Nb_2O_{4.9\pm0.3}$ after, taking into account the uncertainties, in accordance with expected Nb_2O_5 theoretical stoichiometry. Moreover, between 1 and 1.5 MeV energy range, we observe a very weak peak intensity attributed to the signature of the Ar atoms. We believe that the Ar peak originates from Ar plasma used during sputtering deposition and remains present after films annealing.

To pursue the analysis of films composition, RBS measurements were made for Tb-doped samples annealed at 800 °C with a different power density (PD_{Tb4O7}) of 1.78, 2.07, 2.66, and 3.26 $W.cm^{-2}$, respectively. Peaks attributed to Nb and O were found similar for samples deposited with different PD_{Tb4O7}, while the Tb peak's intensity increases. The

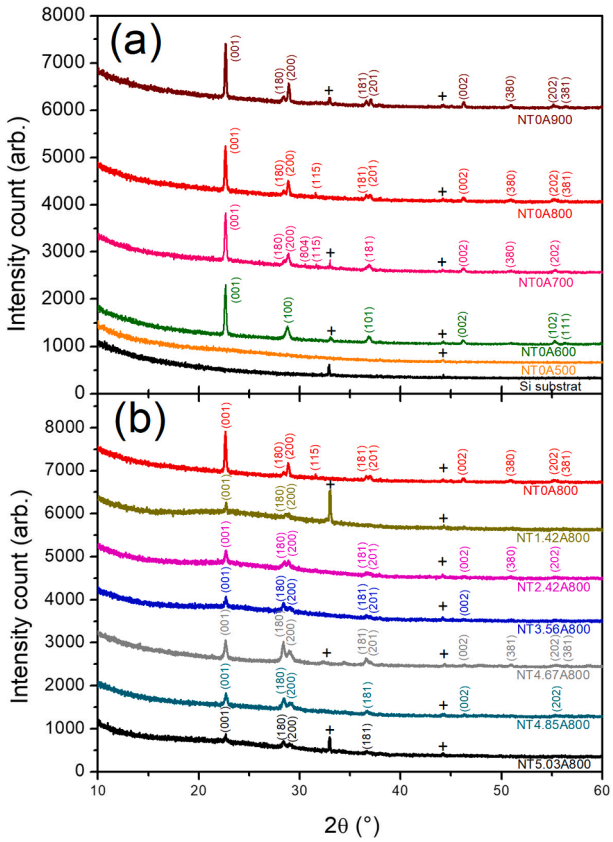

Fig. 3. X-ray diffraction spectra from 10° to 60° with peaks indexation when samples were crystalized of (a) undoped series of Nb2O5, (b) doped series of Nb2O5. The symbol + indicates substrate peaks.

elemental composition of Tb-doped Nb_2O_5 thin films was estimated by fitting the RBS profile displayed in Fig. 1(b). It was found, after taking into account the uncertainties, that stoichiometry of Tb-dope Nb_2O_5 ± 0.4 is comparable with the one of undoped samples and close to, the theoretical stoichiometry of the Nb_2O_5 material. The determination of the Tb^{3+} ion concentration as a function of the target power density PD_{Tb4O7} is displayed in Fig. 2. The elemental composition in Tb of the samples with the PD_{Tb4O7} of 2.36 and 2.96 $W.cm^{-2}$ was obtained by linear interpolation, marked by two red points in Fig. 2. It is seen that Tb^{3+} ion concentration linearly increases with the power density PD_{Tb4O7} up to 2.66 $W.cm^{-2}$ resulting in 4.67 at.% of Tb content, followed by Tb^{3+} ion concentration saturation approaching 5 at.% for higher PD_{Tb4O7}. The variation of power density applied on the Tb_4O_7 target affects logically the proportion of RE incorporation but surprisingly does not affect the O concentration, which was found constant.

Following the determination of the stoichiometry of the undoped and doped samples we name the set of samples by the following nomenclature, N for Nb_2O_5, then T followed by its atomic concentration in at.% and A for the RTA annealing followed by its temperature in degrees Celsius. As an example, with this nomenclature, sample NT0A000 means unannealed and undoped Nb_2O_5 sample while NT4.67A800 means Nb_2O_5:Tb sample with 4.67 at.% of Tb annealed at 800 °C.

The undoped samples were characterized by XRD, leading to the XRD diagrams shown in Fig. 3. In Fig. 3(a), no diffraction peaks were detected for the unannealed sample NT0A000 and annealed NT0A400 and NT0A500 samples. This indicates the amorphous character of Nb_2O_5's samples NT0A000 and NT0A500. For samples annealed between 600 °C and 900 °C (see Fig. 3(a)), respectively NT0A600, NT0A700, NT0R800, and NT0A900, some diffraction peaks were detected with a slight position variation with annealing temperature (T_A). For sample NT0A600, the diffraction peaks match with the pseudohexagonal phase (TT-Nb_2O_5) reference pattern (JCPDS file no.: 00–028-031[32,33]), where lattices parameters are a = b = 3.607 Å, c = 3.925 Å. These observations are confirmed by several authors who determined the threshold T_A of the amorphous to crystalline transition in the TT-Nb_2O_5 crystalline phase after annealing at 500 °C [31] or after annealing at 500–600 °C [3,31]. For the samples further annealed between 700 °C and 900 °C, the diffraction peaks match with reference pattern (JCPDS files no.: 00–030-0873[31,32]) corresponding to the orthorhombic phase (T-Nb2O5), whose lattice parameters are a = 6.175 Å, b = 29.175 Å, and c = 3.93 Å. All measured and reference peak positions are reported in Table A.1 in Appendices.

The XRD spectra obtained for undoped and doped films with varying Tb^{3+} ion concentrations and annealed by RTA at 800 °C are shown in Fig. 3(b). We observed diffraction peaks at identical positions for undoped and doped samples. These peaks are attributed to the T-Nb_2O_5 orthorhombic phase as previously found and confirmed for the undoped samples [32,34]. All XRD measured and reference peak positions are reported in Table A.2 in Appendices.

TEM investigations were performed for undoped and doped samples annealed at 800 °C. Fig. 4 shows cross-sectional views of the selected undoped (Fig. 4(a)) and Tb-doped (Fig. 4(b)) Nb_2O_5 film deposited on Si substrate in bright and dark field modes. Typically, a Nb_2O_5 film of

Table 1
TL1 parameters obtained by fitting URA reflectance and VASE measurements for NT0A800 sample. The Δ is the relative difference between these two experimental measurements.

TL1 parameters	URA fit	VASE	Δ (%)
E_g	3.049	3.044 ± 0.021	0.1640
ε_∞	3.075	3.072 ± 0.065	0.0976
A	109.521	109.387 ± 3.926	0.1223
E_0	4.992	4.999 ± 0.026	0.1402
C	2.370	2.378 ± 0.066	0.3375
Thickness (nm)	154.78	152.274 ± 1.991	1.6191

Table A1
Indexing of annealed Nb_2O_5 NT0A600 for XRD measurements with JCPDS reference used for phase identification for TT-Nb_2O_5.

2θ	JCPDS file no.: 00–028-031 TT-Nb_2O_5 pseudohexagonal		
NT0A600	2θ	d (A)	hkl
22.63	22.607	3.925	(0 0 1)
28.78	28.587	3.124	(1 0 0)
36.87	36.712	2.446	(1 0 1)
46.19	46.234	1.962	(0 0 2)
55.26	55.187	1.660	(1 0 2)
56.37	56.141	1.637	(1 1 1)

Table A2
Indexing of annealed Nb_2O_5 NT0A700, NT0A800, and NT0A900 for XRD measurements with JCPDS reference used for phase identification for T-Nb_2O_5.

2θ			JCPDS files no.: 00–030-0873 T-Nb_2O_5 orthorhombic		
NT0A700	NT0A800	NT0A900	2θ	d (A)	hkl
22.64	22.63	22.66	22.061	3.930	(0 0 1)
28.44	28.41	28.43	28.401	3.140	(1 8 0)
28.89	28.83	28.92	28.890	3.088	(2 0 0)
30.53	–	–	30.168	2.960	(8 0 4)
31.60	31.65	–	31.937	2.800	(1 1 5)
36.92	36.58	36.59	36.604	2.453	(1 8 1)
–	37 0.01	37 0.09	36.994	2.428	(2 0 1)
46.25	46.21	46.30	46.159	1.965	(0 0 2)
51.01	51.01	51.00	50.89	1.793	(3 8 0)
55.38	55.17	55.13	55.368	1.658	(2 0 2)
–	56.44	56.31	56.37	1.631	(3 8 1)

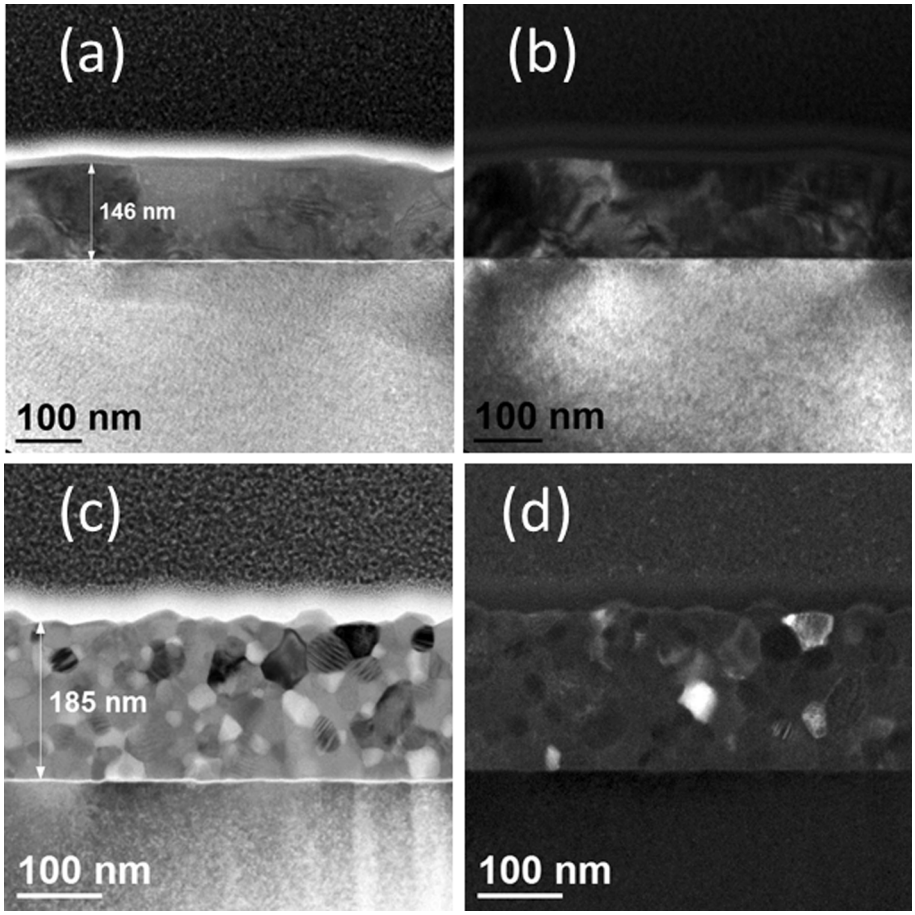

Fig. 4. (a) Bright-field and the corresponding (b) dark-field TEM images of the undoped sample (NT0A800) and (c) bright-field and the corresponding (d) dark-field TEM images of a doped sample (NT4.67A800). The images were taken with the electron beam parallel to the [1 1 0] direction of Si.

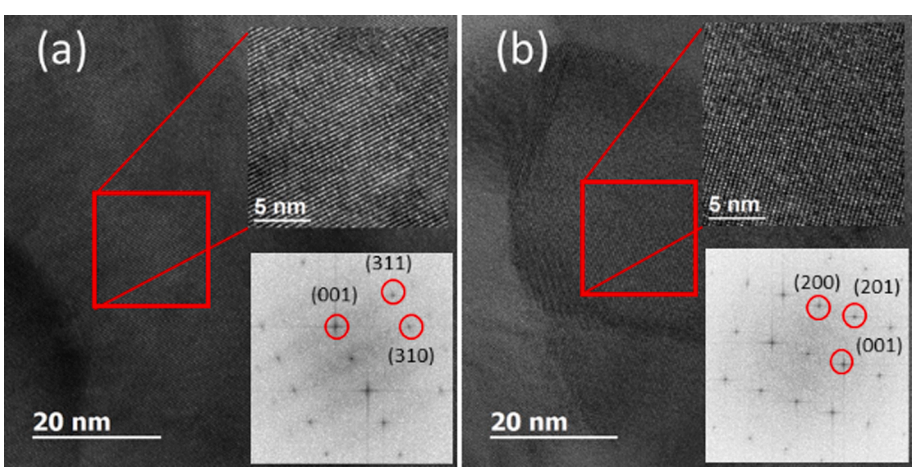

Fig. 5. (a) HRTEM image NT0A800, with enlargement of the red squared region associated with Fast Fourier Transform of image. (b) HRTEM image of NT4.67A800, with enlargement of the red squared region associated with Fast Fourier Transform of image.

variable thickness beetwen 140–150 nm range surmounting at a thin silica layer of 3 nm and the silicon substrate is observed. The Nb_2O_5 film thickness fluctuation is due to a significant roughness at the film surface. The Bragg contrast seen in darkfield mode in the film (see Fig. 4(b)), indicates the presence of various crystalline orientations or, in general, material phase nature. The large grains with a diameter of several hundred nanometers lying parallel to the substrate are also well visible. TEM micrographs made in the cross-sectional view of NT4.67A800 film are presented with bright field mode in Fig. 4(c) and dark field mode in Fig. 4(d), respectively. The cross-section views show a film of about 185 nm thick with a multicrystalline structure with an observable grain size ranging from 10 to 70 nm. Moreover, no texture or no obvious orientation relationship between the grains is observed. Some empty voids are also found in the film with a size comparable to the smallest grains. Also, a thin silica layer of a few nanometers at the film/substrate interface is visible for the undoped film.

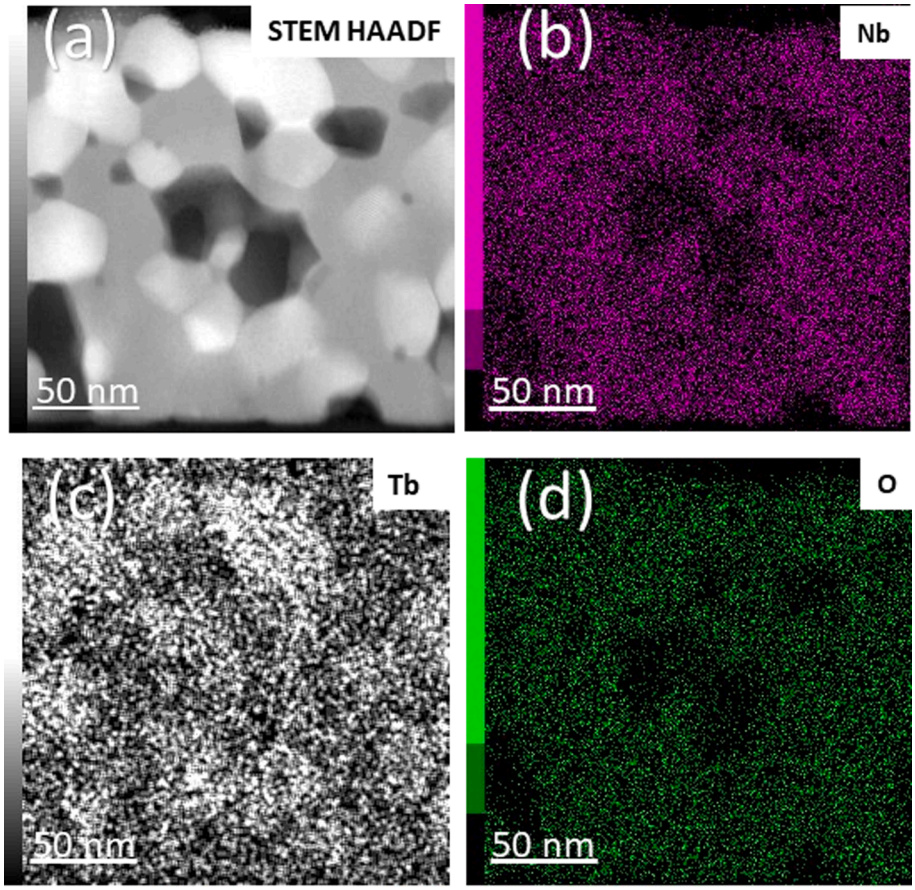

Fig. 6. (a) STEM HAADF image of the NT4.67A800 grown on Si. Chemical maps of Nb (b), Tb (c), and O (d) elements.

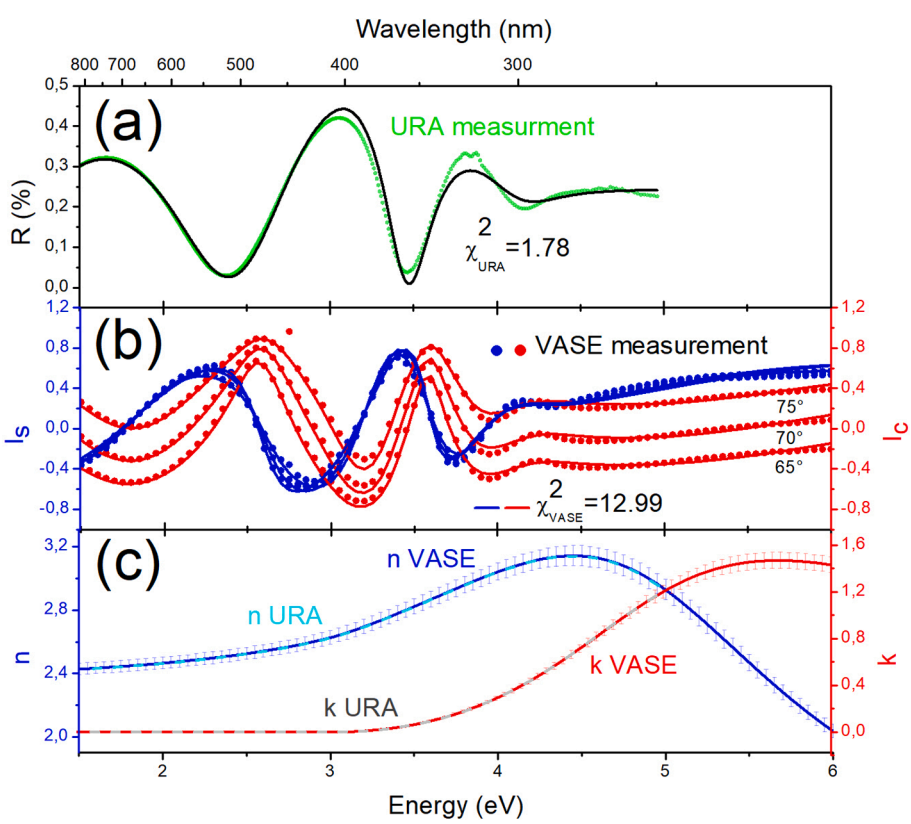

Fig. 7. Optical measurement conducted for NT0A800 sample: (a) spectrum of reflectance measured by URA at 8° of incidence in TE polarization represented in green dot-line, the black line is the result of fitting with TL1 model simple oscillator calculated in the same condition (χ^2_{URA} = 1.78). (b) Is et Ic spectra measured with VASE equipment with three incident angles for blue and redpoint lines respectively and the corresponding fits on DeltaPsi2 software with TL1 model (χ^2_{VASE} = 12.99). (c) n and k spectra between 1.5 V and 6 eV deduced from URA (green dot-line Fig. 7(a)) and VASE (blue and red dot-lines Fig. 7 (b)) measurements with error bars.

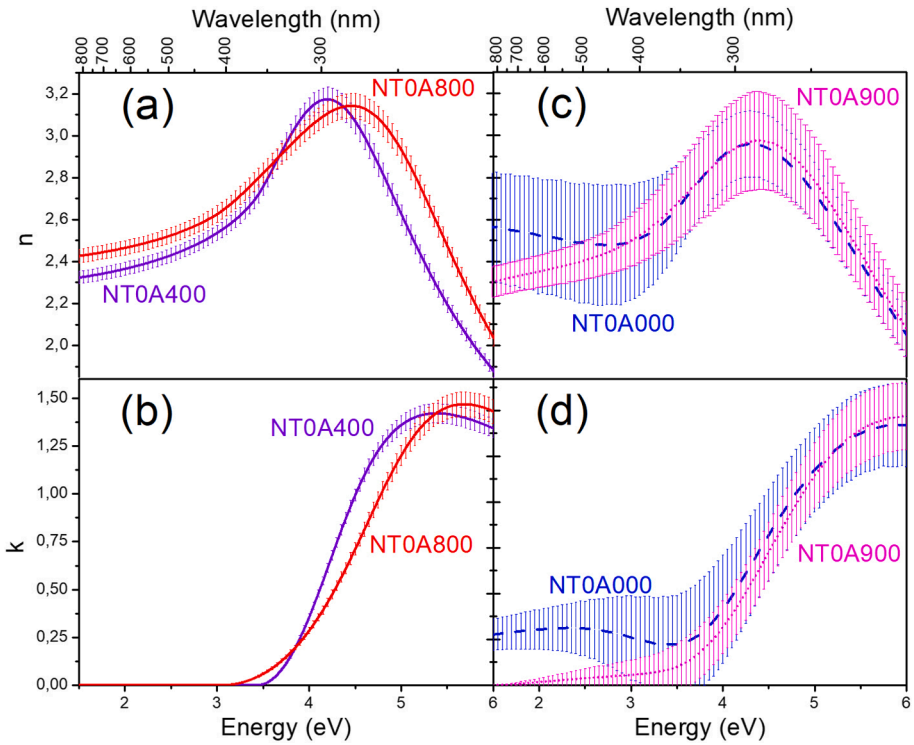

Fig. 8. (a) (c) The refractive index n as a function of energy obtained with variable angle ellipsometry spectroscopic and (b) (d) the extinction coefficient k as a function of energy with error bar for the samples respectively (a) (b) undoped annealed at 400 °C and 800 °C. (c) (d) samples undoped unannealed and annealed at 900 °C.

The HRTEM investigations were made on undoped and doped samples annealed at 800 °C. Fig. 5(a) is a typical HRTEM image of a large single crystal region of the NT0A800 film that shows several lattice planes. The lattice magnification shown in Fig. 5 reveals two planes families perpendicular to each other. The Fast Fourier Transform (FFT) of Fig. 5(a) is consistent with a $[1\bar{3}0]$ projection of the T-Nb_2O_5 orthorhombic phase and therefore confirms its orthorhombic structure.

Fig. 5(b) is a typical HRTEM image of the NT4.67A800 showing a large crystallite. An enlargement of a central region of the crystallite seen in Fig. 5(b) shows different families of lattice planes of the niobium oxide. The FFT of Fig. 5(b) is consistent with a [0 1 0] projection of the T-Nb_2O_5 orthorhombic phase. Also small grains, not shown here, were found after FFT with projection consistent with TT-Nb_2O_5 or P-Nb_2O_5 (tetragonal phase)[35]. Due to the low volume fraction of those minority phases, the XRD diagram did not show the corresponding peaks.

STEM HAADF micrographs for NT4.67A800 sample are presented in Fig. 6. Fig. 6(a) shows a STEM HAADF image with various contrasts between grains confirming different chemical compositions present. The darkest regions are the empty cavities in the films. The Nb and O element composition maps shown ion Fig. 6(b),(c) have, fewer counts in selected areas corresponding to empty cavieties (*e.i.* dark spots in Fig. 6 (a)). It is interesting to note that the grains seen as brightest spots on the Tb map (Fig. 6(c)) contain larger Tb content indicating non-uniform Tb distribution in the fim. The overall Tb concentration in the film measured by EDX is close to 5.6 at.% which is in good agreement with the values obtained from RBS analysis which is less sensitive to detect local dopant distribution fluctuation. Indeed, the brightest grains seen in Fig. 6 have a Tb content of up to 18.5 at.% whereas the gray ones have only 1.1 at.%, respectively. These fluctuations in Tb composition from grain to grain may induce changes in the expected dominance of orthorhombic Nb_2O_5 phase by a mixture of other phases for a specific T_A as observed in TEM.

3.2. Optical properties

The refractive index n and the extinction coefficient k are the main parameters to characterize a linear optical material. The complex refractive index (e.i. $n + ik$) was investigated using two complementary techniques described in the Material and Methods: first, optical reflectance measurement using URA, and second Ellipsometer using VASE. Indeed, the first method is based on intensity measurement, while the second is based on polarization rotation measurement. These complementary characterization methods have been performed on an NT0A800 sample to validate the use of the VASE method for the following part of this work. Fig. 7 shows measured reflectance displayed as black dot-line. Using the developed fitting routine we have computed the reflection, transmission, and absorption spectra of a specific material layer described by the Tauc-Lorentz dielectric function single oscillator model (TL1) as previously described. Here, the Nb_2O_5 thin film is considered homogenous and overlapped by a composite layer of Nb_2O_5 and air to simulate the roughness with the effective medium approach. As seen in Fig. 7(a), the black line is the result of the fitting corresponding to the best chi-squared function value ($\chi^2_{URA} = 1.78$) obtained by fitting the URA reflectance measurement. Fig. 7(c) displays the n and k coefficients deduced from this fit.

In addition to the URA approach, ellipsometric measurements (VASE) have also been carried out for the undoped NT0A800 sample. The experimental data I_c and I_s were fitted by adjustable parameters of Tauc-Lorentz's model (see Fig. 7(b)) and thickness. As previously mentioned, the Nb_2O_5 thin film was considered homogenous and overlapped by an interface layer composed of Nb_2O_5 film and air to simulate the roughness with the EM approach. The URA reflectance fitting parameters and VASE measurement TL1 parameters along with estimated film thicknesses are displayed in Table1. The n and k curves, deduced from fitting parameters of Tauc-Lorentz's model are shown in Fig. 7(c). A good agreement between these two complementary approaches appears through the overlapping of n and k curves in Fig. 7(c). To compare

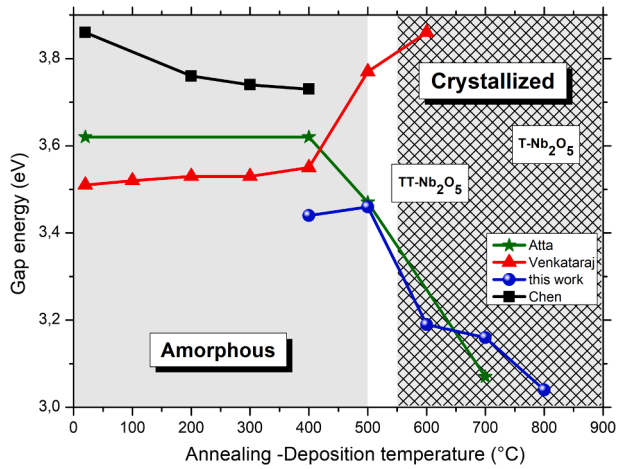

Fig. 9. Bandgap energy as a function of annealing temperature T_A (Venkataraj et al.[31], Atta et al.[38], this work,) or deposition temperature (Chen et al. [42]). Grey areas illustrate the different phases according to the T_A.

the parameters in table 1, the relative-parameters difference is calculated as follows.

$$\Delta = 100 \times \frac{|P_{iVASE} - P_{iVURA}|}{P_{iVASE}} \quad (2)$$

where P_{iVASE} and P_{iURA} correspond to TL1 parameters obtained by fitting VASE and URA data, respectively. For all parameters considered, the relative difference Δ is less than 1%, reflecting a good agreement between these two complementary methods.

Based on the above presented analysis we believe that the dielectric function TL1 accurately describes the optical linear properties of the Nb_2O_5 samples. Furthermore, the reflectance measurement confirms the results obtained with the VASE model using the ellipsometric technique. Consequently, VASE measurements and analysis using three incident angles (*i.e.* 65°, 70°, and 75°) are systematically applied hereafter.

All undoped Nb_2O_5 samples, both unannealed and annealed at various T_A temperatures with 100 °C increments up to 900 °C were measured by VASE technique. Samples were considered as homogeneous layers, however for samples annealed between 700 °C and 900 °C an additional interface layer was considered due to the surface roughness change with the T_A increase. Corresponding refractive index and extinction coefficient dispersion were described by either a single oscillator Tauc-Lorentz (TL1) model for samples annealed between 400 °C and 800 °C or a double oscillator Tauc-Lorentz (TL2) model was used for the unannealed samples and one annealed at 900 °C. Fig. 8(a) and (b) display the corresponding *n* and *k* spectra of the NT0A400 and NT0A900 samples with estimated error bars. The *n* and *k* spectra comparably evolve with energy to those of the ones of Nb_2O_5 material reported by Gao et al.[36,37]. The refractive index values in the visible and UV are similar to those reported in the literature [23,31,38] for material deposited using a RF sputtering technique. The extinction coefficient value is close to zero over the energy range 1.5 eV to 3 eV then increases to a maximum after 5 eV. Furthermore, one may notice that the *n* and *k* maxima blue shift with T_A change from 400 °C to 800 °C.

Fig. 8(c) and (d) show the n and k spectra of the two extreme samples of the set, unannealed and annealed at 900 °C. As explained above, these samples turned out to be different, as a TL2 dual oscillator model was required, as opposed to the other samples described by a TL1 single oscillator model. As already mentioned, these samples turned out to be different, as far as the TL2 dual oscillator model was considered, in contrast to the remaining samples well described by a TL1 single oscillator model. As seen in Fig. 8 the refractive index *n* spectra, as well as the extinction coefficient k spectra evolved as compared to their counterpart shown in Fig. 8(a) and (c). The last one clearly shows a higher

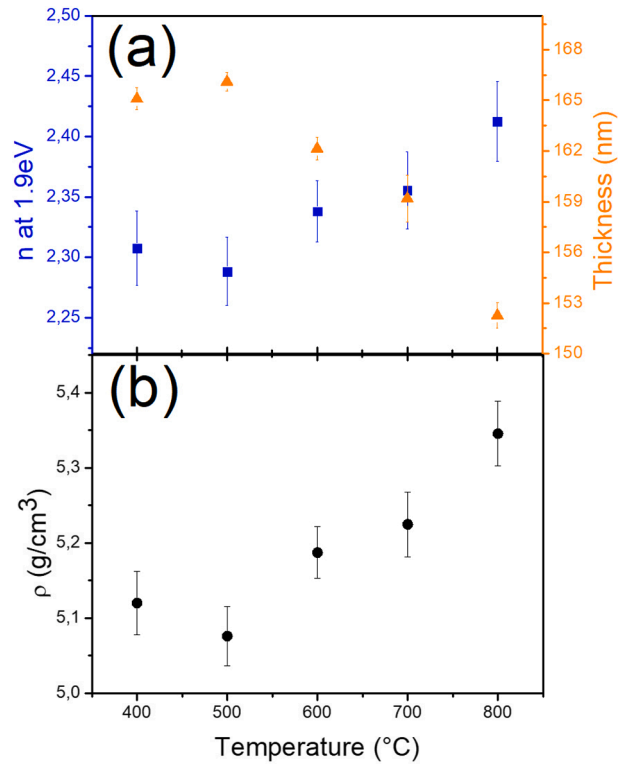

Fig. 10. (a) Refractive index n (at 1.90 eV) evolution with T_A for samples annealed between 400 °C and 800 °C(blue squares) and Nb_2O_5 film thickness (orange triangles), obtained with VASE function T_A. (b) Calculated Nb_2O_5 density ρ with error bars.

absorption coefficient in a range of 1 eV to 3.5 eV. The absorption change between the unannealed Nb_2O_5 and annealed at 900 °C films can be related either to chemical differences or to structural modifications of the Nb_2O_5 film induced by annealing. The RBS measurements showed no change in stoichiometry between unannealed and annealed at 800 °C samples. However, the XRD analysis demonstrated a continuous Nb_2O_5 structural evolution with the annealing temperature varying from amorphous (including unannealed samples and annealed up to 500 °C) to TT-Nb_2O_5 phase (including samples annealed between 500 °C and 650 °C) and T-Nb_2O_5 phase (including annealed samples between 700 °C and 900 °C).

Furthermore, to analyze the values obtained for a single oscillator dielectric function model we selected the bandgap energy (E_g) parameter of the single oscillator TL1 model. Consequently, the E_g values for samples annealed at T_A varying between 400 °C and 800 °C are considered and presented in Fig. 9. These E_g energies vary from 3.4 eV to 3.0 eV with the increasing T_A. In the literature, the E_g energy, among others, depends on the nature of the material, growth method, substrate, annealing technique, but also on how the measurement is interpreted in terms of structural and dielectric models. Different authors[13,39–41] reported Nb_2O_5 bandgap energy to be in a similar energy range from 3 eV to 4 eV but its evolution with T_A exhibited a different trend. Fig. 9 shows the evolution of Eg as a function of T_A [31,38] or deposition temperature[42] of Nb_2O_5 films synthesized by similar/comparable sputtering methods.

In this work, we observed that bandgap energy decreases with the T_A with an abrupt descent corresponding to the transition from amorphous to crystallized phases. Atta et al.[38] have also observed such a decrease in a similar temperature range. Also, Chen et al.[42] have reported a decreasing of the bandgap energy with T_A while remaining under 400 °C and therefore in the amorphous phase. On the other hand, surprisingly Venkataraj et al.[31] observed the opposite behavior with an almost constant bandgap energy value followed by its increase almost at the

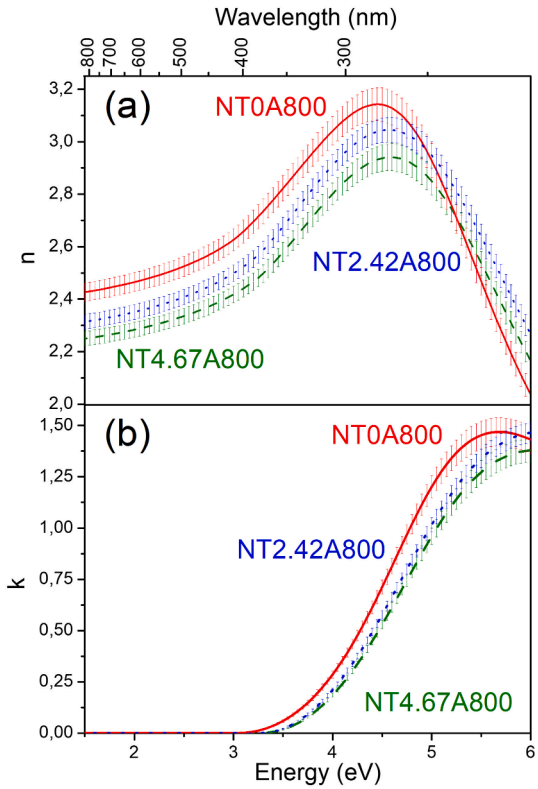

Fig. 11. (a) Refractive index n as function of energy obtain with variable angle ellipsometry spectroscopy for NT0A800 (red line), NT2.42A800 (blue line) and NT4.67A800 (green lne) samples. (b) Absorption coefficient k as function of energy for the same samples. All curves are plotted together with uncertainty error bars.

transition between the amorphous and crystallized phases.

Subsequently, we selected results obtained for T_A ranging from 400 °C to 800 °C where a single Tauc-Lorentz oscillator model was used. The refractive index n selected at 1.90 eV (652 nm) because of the negligible extinction coefficient value and the film thickness are reported in Fig. 10(a). We observed that the n@1.90 eV value is slightly decreasing for T_A varying from 400 to 500 °C and then followed by a monotonic increase close to 8% while the film thickness is first slightly increasing followed by a 8% decrease. Such antagonistic behaviors of refractive index n and thickness with T_A have already been observed in at least two studies, which related the variation of the density of the materials with the T_A[23,31]. To further investigate this fact, we estimate the Nb_2O_5 density ρ, using the Lorentz-Lorenz law[43] which links the refractive index n and the density ρ given by the following formula:

$$\frac{n^2-1}{n^2+2} = \frac{4}{3}\pi\alpha_m\rho\frac{N_A}{M} \tag{3}$$

where α_m is the molecular electronic polarizability, N_a is Avogadro constant and M is the Nb_2O_5 molecular weight equal to 265.81 g.mol^{-1}, respectively. In the current case, we consider only the electronic polarizability at 1.90 eV (652 nm). The molecular electronic polarizability α_m could be expressed as the sum of electronic polarizability of individual ions[44] as $\alpha_m = A\alpha_+ + B\alpha_{m-}$, where A and B are the stoichiometric factors and α_+ and α_- are the electronic polarizabilities of Nb^{5+} and O^{2-} respectively. In the literature, these values are $\alpha_+ = 0.076 \times 10^{-24} cm^3$ [45] and $\alpha_- = 2.4 \times 10^{-24} cm^3$ [46], and the molecular electronic polarizability is found to be $\alpha_m = 12.15 \times 10^{-24} cm^3$, respectively.

To determine the molecular electronic polarizability α_m, we initially relied upon the data obtained from the relationship $\frac{n^2-1}{n^2+2} = f(\rho)$ presented by Venkataraj et al. [31]. However, according to the formula (1), the variation of $\frac{n^2-1}{n^2+2}$ vs. ρ requires passing through the origin point, which surprisingly was not made by the authors. The linear fit passing by the origin point led us to the determination of $\alpha_m = 13.1081 \pm 0.4025 \times 10^{-24} cm^3$ in accordance with the value previously obtained from literature instead of the Venkataraj et al value of $\alpha_m = 6.327 \times 10^{-24} cm^3$. Using this $\alpha_m = 13.1081 \pm 0.4025 \times 10^{-24} cm^3$ and the formula (1), we have determined the ρ value as a function of annealing temperature T_A as shown in Fig. 7(b).

Evolving like the variation of the refractive index with the annealing temperature T_A, the density values obtained remain in the density range

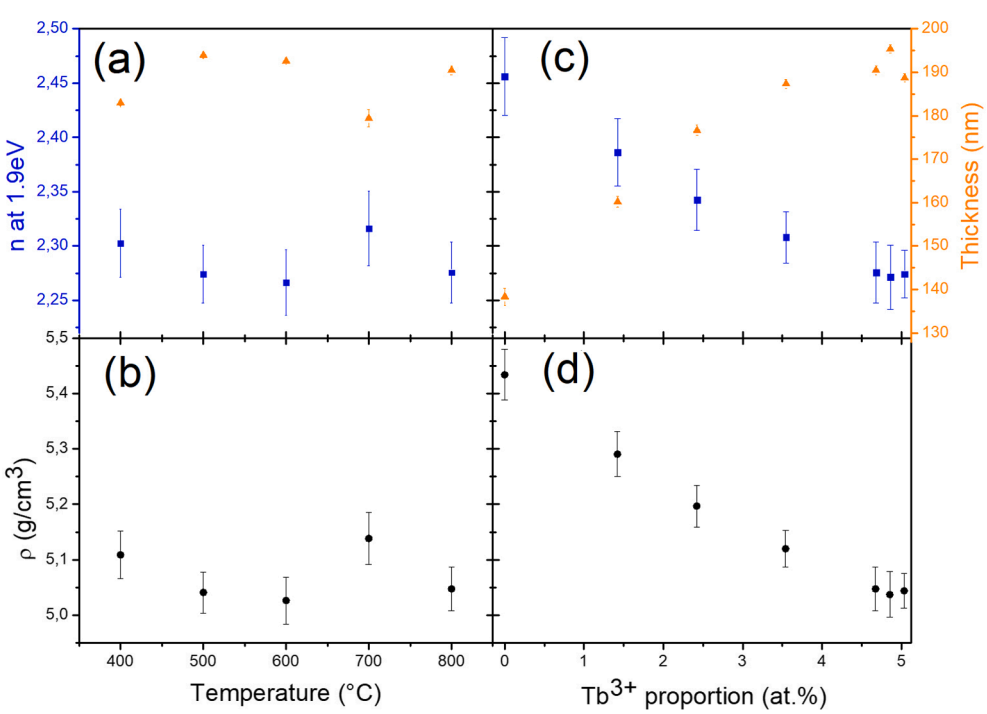

Fig. 12. (a) and (b) Evolution of Tb-doped Nb_2O_5 refractive index n at 1.90 eV and film thickness measured with VASE and calculated material density for sample doped with 4.67 at.% of Tb as a function of T_A temperature. (c) and (d) Evolution of Tb-doped Nb_2O_5 refractive index n at 1.90 eV and film thickness measured with VASE and calculated material density and calculated material density for samples annealed at 800 °C. Symbols in panels are: refractive index (blue square), films thickness (yellow triange) and matrial density (black circle).

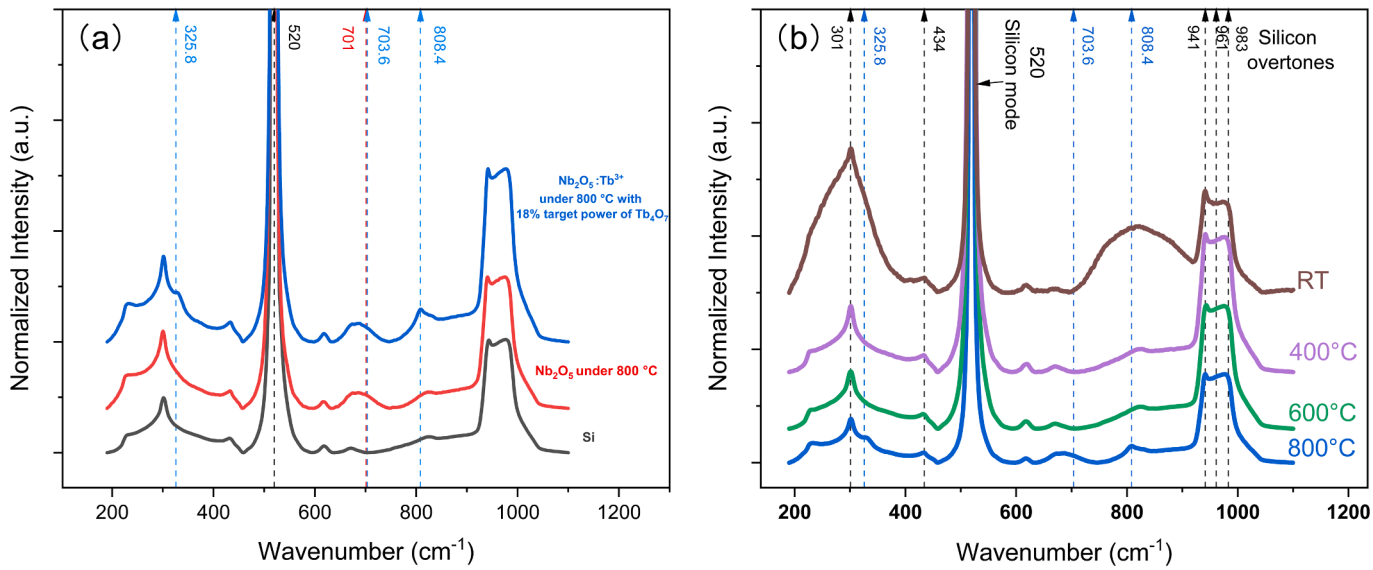

Fig. 13. (a) Raman spectra of Si (1 0 0) p-type substrate, undoped Nb_2O_5 thin film annealed at 800 °C (NT0A800), and Tb-doped Nb_2O_5 thin film annealed at 800 °C (NT4.67A800). (b) Raman spectra evolution for Tb-doped Nb_2O_5 thin films having the same Tb content and annealed at different temperatures (NT4.67A000, NT4.67A400, NT4.67A600, and NT4.67A800).

of 4.70 to 4.95 g.cm^{-3} in good agreement with those obtained in literature[31]. First, a slight decrease from 4.75 to 4.70 g.cm^{-3} for annealing temperature varying from 400 °C to 500 °C was observed, followed by a monotonic increase up to 4.95 g.cm^{-3} for $T_A = 800$ °C. This significant density increase occurs simultaneously with a decrease in the film thickness. Such densification of the film is concomitant with the structural modifications from amorphous to crystalline phase observed by the XRD measurements showing that the Nb_2O_5 samples annealed at 400 and 500 °C remain amorphous whereas for samples annealed between 600 °C and 800 °C, the crystallized phases TT, then T are observed, respectively.

Fig. 11(a) and 11(b) show n and k spectra respectively for the first three samples NT0A800, NT2.42A800, and NT4.67A800 annealed at 800 °C. The shape of the spectra does not differ significantly from ones observed for the undoped samples, however, some dependence of n value on Tb^{3+} ion concentration is evidenced. Indeed, it can be seen that in 1 eV to 3 eV region where absorption is equal to zero ($k = 0$) the n value decreases when the Tb^{3+} ion content increases. It shall be mentioned that for the NT0A800, NT2.42A800, and NT4.67A800 samples which have a very close Tb content, both n and k retain similar values (not shown) in agreement with the uncertainties.

The bandgap energy (Eg) values obtained for doped annealed samples are reported in Table B.1 in Appendice. The Eg values were determined using a single oscillator TL1 model for all doping and T_A ranging from 400 to 800 °C, while a double oscillator TL2 model was used for an annealed sample at 900 °C, respectively. It was found that the E_g does not change with Tb content increase while the E_g decreases with annealing temperature T_A. Specifically, the E_g value is the range between 3.35 eV − 3.55 eV for T_A ranging from 400 °C to 600 °C, then in the range 3.3 eV − 3.4 eV for T_A of 700 °C, and then deacreses to 3.1 eV − 3.3 eV for T_A of 800 °C and 2.6 eV − 2.9 eV for samples annealed T_A of 900 °C. The bandgap energy decrease with the T_A annealing temperature for the Tb-doped samples is comparable to that observed for the undoped samples, where such E_g change was accompanied by a structural transformation from an amorphous phase to successive crystallized phases.

The density ρ values for Tb-doped Nb_2O_5 were determined with a similar approach as for the undoped Nb_2O_5 sampes. The refractive index n at 1.90 eV, Tb-doped films thickness, and calculated density ρ values are represented as a function of T_A for a selected Tb concentration of 4.67 at.% are shown in Fig. 12(a) and (b). Surprisingly, and contrary to the results for undoped samples, the refractive index, the thickness, and the density ρ are quasi constant with T_A. The n value is close 2.3 at 1.9 eV incident photon energy, similarly to the one of the amorphous undoped sample. Also, the density ρ value (4.70 gcm^{-3}) does not change and remains relatively unchanged for all Tb-doped samples. However, this value is smaller than the one found for the undoped sample annealed at 800 °C (4.95 gcm^{-3}) corrabortating a Nb_2O_5 material structural modification due to the Tb doping.

Fig. 12(c) and (d) shows the refractive index n at 1.90 eV, the Tb-doped film thickness, and calculated Nb_2O_5 density as a function of Tb^{3+} ion concentration for T_A of 800 °C, respectively. It is seen that the refractive index value decreases with the increasing Tb content while the film thickness increases. Accordingly, the n value at 1.90 eV decreases from 2.46 to 2.27 as well as the calculated density ρ values decreases from 5.05 g.cm^{-3} to 4.66 g.cm^{-3}. Thus, Tb-doped Nb_2O_5 density decreases at the same time as film thickness increases with Tb doping. Therefore, we conclude that Tb incorporation seems to make the Nb_2O_5 film less dense and relatively thicker due to the formation of void cavities as observed in TEM and STEM-HAADF analysis for NT4.67A800 film. Furthermore, VASE measurements confirmed that Nb_2O_5 films became less dense and thicker with increasing Tb content for a given T_A temperature.

3.3. Raman spectroscopy

Fig. 13 shows Raman spectra of Si substrate, reference Nb_2O_5 film (NT0A800), and Tb-doped Nb_2O_5 film (NT4.67A800), respectively. It is seen in Fig. 13(a) that the main Si peak for all samples is located at ~ 520 cm^{-1}. In brief, the Si sample was used as a gauge whereas a distinct Raman band associated with Nb_2O_5 at 701 cm^{-1} (red dashline) arises from the deconvolution procedure of the Raman specrum for reference undoped Nb_2O_5 thin film annealed at 800 °C as shown in Figure C.1. in Appendices. The Tb-doped Nb_2O_5 thin film shows three distinct Raman peaks at 325.8 cm^{-1}, 703.6 cm$^{-1,}$ and 808.4 cm^{-1}, respectively. The Nb_2O_5 related Raman peak at 701 cm^{-1} is shifted to 703.6 cm^{-1} due to the Tb doping process. According to Dash *et al.* [47] the Raman spectrum of Nb_2O_5 thin film grown on Si substrate shows five peaks at 238 cm^{-1}, 304 cm^{-1}, 647 cm^{-1}, 695 cm^{-1}, and 993 cm^{-1}, respectively. In our case due to the very strong Si substrate background signal, only the peak near 695 cm^{-1} was considered and unambiguously determined by the deconvolution process. This peak corresponds to a transverse optical

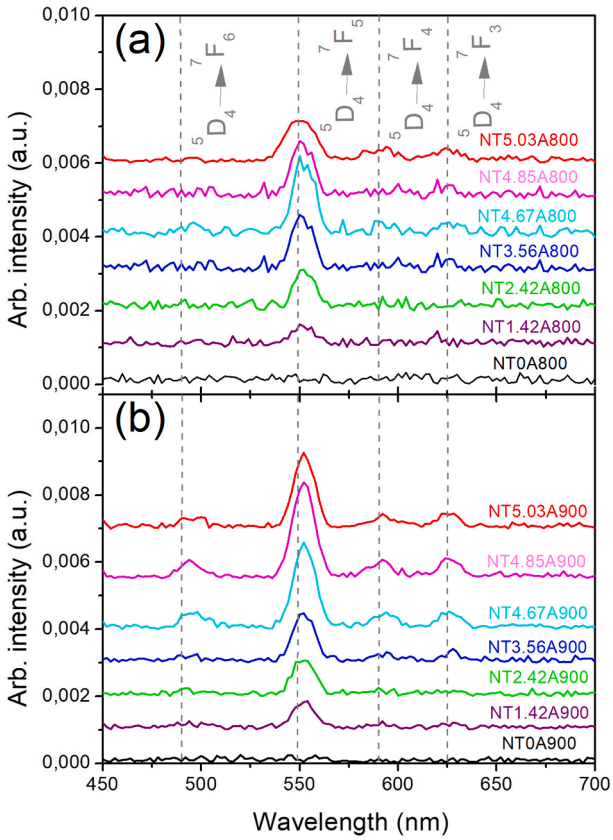

Fig. 14. PL spectra for Tb-doped Nb_2O_5 films doped with Tb concentration between 0 at.% to 5.03 at. % and annealed at (a) 800 °C and (b) 900 °C.

(TO) mode (doubly degenerated) which is related to the stretching mode of NbO_6 polyhedral typically observed in the Nb_2O_5 orthorhombic phase [47–49]. In our case, Raman spectrum deconvolution gives a peak at 701 cm^{-1} which is red-shifted concerning the peak at ~ 690 cm^{-1}. As reported by Zhou *et al.* [50], this redshift can be induced by the interaction between Si substrate and orthorhombic phase Nb_2O_5 film. Furthermore, peaks at ~ 325.8 cm^{-1} and ~ 808.4 cm^{-1} only seen for Tb-doped Nb_2O_5 thin film are due to the presence of Tb^{3+} ion in the host lattice. It has been established from TEM and XRD studies that the thin films of Nb_2O_5 undergo a significant phase change with T_A, remaining amorphous after annealing at 400 °C and 500 °C, then mostly pseudo-hexagonal (TT-Nb_2O_5) at 600 °C, then mainly orthorhombic (T-Nb_2O_5) for 700 °C to 900 °C annealing temperatures. Therefore, to get better inside into the annealing effect on Tb-doped Nb_2O_5 thin films evolution, the Raman spectra of unannealed and selected annealed samples are shown in Fig. 13(b). All spectra shown were collected for the same Tb concentration (4.67at.%), normalized, and shifted up for clarity. Fig. 13 (b) shows peaks at 301 cm^{-1}, 434 cm^{-1}, 520 cm^{-1}, 610 cm^{-1}, 670 cm^{-1},941 cm^{-1}, 961 cm^{-1}, and 983 cm^{-1} identified as typical Si bands [51]. Only an unannealed Nb_2O_5:Tb^{3+} sample shows distinct broadband at ~ 808.4 cm^{-1} which changes with increasing T_A and merges with Raman spectra background level for the sample annealed at 800 °C. For Tb-doped Nb_2O_5 samples annealed at 400 °C and 600 °C, there are no significant Raman peaks position change observed due to Tb doping. Finally, for the Tb-doped Nb_2O_5 sample annealed at 800 °C, three distinct Raman peaks have appeared at 325.8 cm^{-1}, 703.6 cm^{-1}, and 808.4 cm^{-1}, respectively.

For the Tb-doped Nb_2O_5 thin films with increasing Tb content, the Nb_2O_5 Raman peak shifts from 701 cm^{-1} to 703.6 cm^{-1} as shown in Fig. 13(a). The Raman spectra evolution due to Tb doping was investigated for selected Nb_2O_5 thin films deposited with various Tb content of 1.42*at*.%, 2.42*at*.%, 4.67*at*.%, and 5.03*at*.%, respectively, and annealed at 800 °C. The corresponding Raman spectra are shown in Figure C.1. in Appendices. The deconvoluted Raman spectra show that the Nb_2O_5 peak varies slightly between ~ 702 cm-1 and 704 cm-1 with the Tb concentrations. This shift of Nb_2O_5 peak to higher wavenumbers may indicate

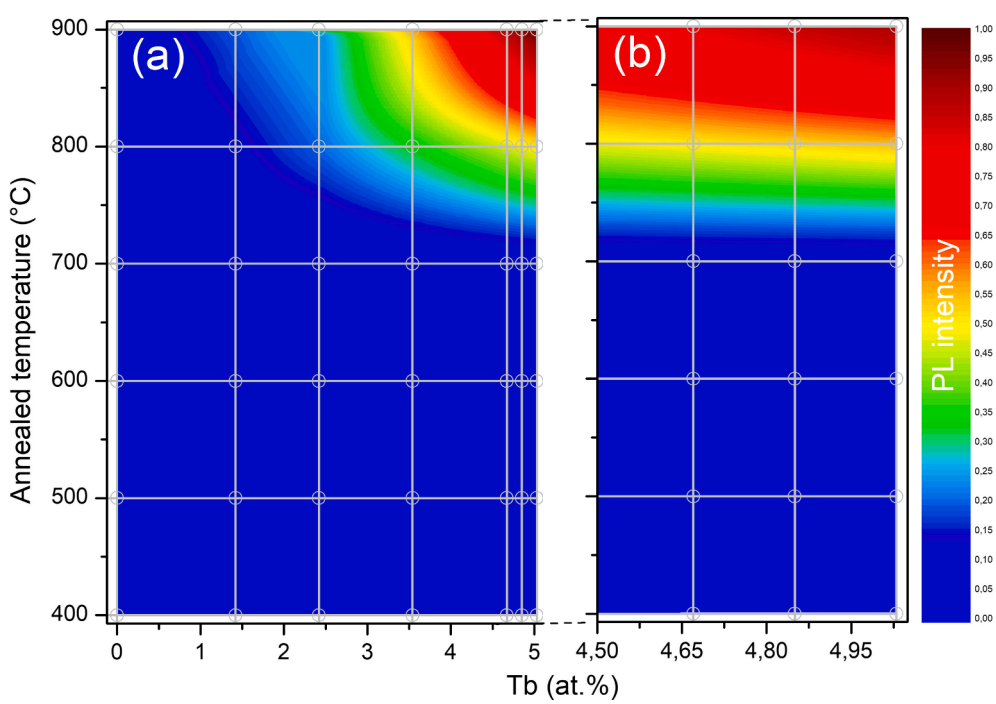

Fig. 15. (a) PL relative intensity map obtained for the $^5D_4 \rightarrow {}^7F_5$ transition line integrated between 530 nm and 570 nm for Nb_2O_5 doped with various Tb content and annealed between 400 °C and 900 °C for all annealed samples as a function of terbium concentration and annealing temperature: (a) in full view and (b) in detail view for the most concentrated.

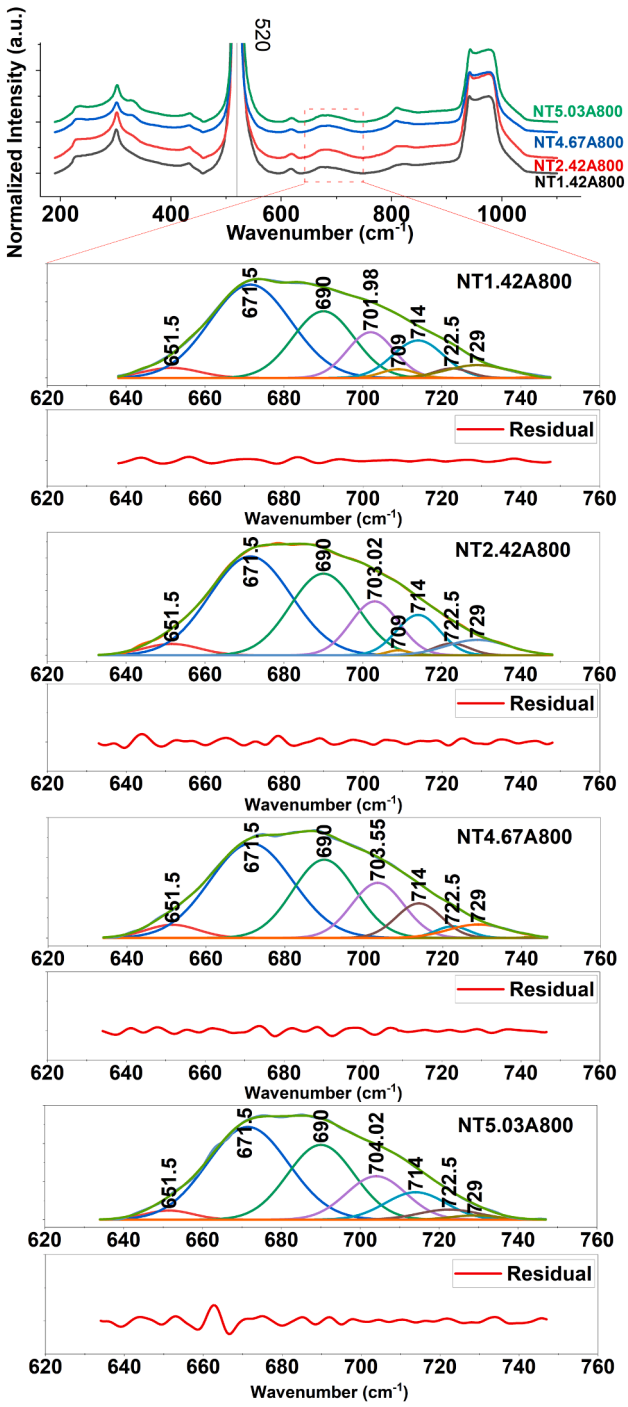

Fig. C.1. (a) The evolution of Raman spectra of Nb_2O_5 doped with different Tb content and annealed at 800 °C. (b) deconvoluted Raman spectra in 620 cm^{-1} to 760 cm^{-1} range with the spectral residual component having coefficients of determination (COD) of 0.999 obtained from Originlab Pro.

that the bond length between ions in the Nb_2O_5 host lattice changed with increasing the Tb content. Indeed, the Tb^{3+} ion substituting for Nb^{5+} ion could form $TbNbO_4$ phase and/or Tb_2O_3 phase, respectively, causing host lattice distortion and subsequent modification of the bond length in the Nb_2O_5 lattice [48,52]. Moreover, there are two supplementary Raman peaks assigned to Tb^{3+} ion seen at ~ 325.8 $cm^{-1}$and ~ 808.4 cm^{-1}. The first one represents a typical doubly degenerate mode for c-type Tb_2O_3 due to the oxygen vibrations and indicates the presence of the c-type Tb_2O_3 grains. The second Raman peak at ~ 808.4 cm^{-1} represents the Tb^{3+} ion vibration in the $TbNbO_4$ phase present in the Nb_2O_5 sublattice. The Raman spectrum, of the unannealed sample, shows broad bands superimposed to the Si Raman signal indicating the existence of the amorphous structure where the NbO_6, NbO_7, and NbO_8 polyhedral are present [48,53]. Samples annealed between 400 °C and 600 °C, show no distinguishable Raman peaks for Nb_2O_5 phase and phases containing Tb^{3+} ion because of the strong Si Raman background. For samples annealed at T_A up to 800 °C, the Raman peaks resulting from better ordered orthorhombic phase structure became more intense and therefore more resolved [48].

3.4. Photoluminescence properties

Photoluminescence (PL) spectra were recorded for undoped and doped samples annealed at several T_A temperatures. PL was detectable only for doped samples annealed at a temperature equal to or>800 °C. Fig. 14 depicts the PL spectra in the visible range. Fig. 14(a) and (b) show the PL spectra with various Tb^{3+} ion contents and annealed at 800 °C and 900 °C, respectively. The most intense peak at 549 nm wavelength, attributed to $^5D_4$ to $^7F_5$ transition of the Tb^{3+}, is detected. Other peaks with lower intensities were identified at around 490 nm, 590 nm, and 625 nm attributed to $^5D_4$ to ^7F_j (j = 6, 4, 3), respectively. Apart from the Tb^{3+} ion bands, no other PL bands were detected for undoped samples (NT0A800 and NT0A900). The PL emission results from radiative recombination resulting from the excited $^5D_4$ level. This energy level is populated either by direct resonant excitation or by non-radiative recombination from upper levels. In our case, by using excitation at 266 nm upper levels of Tb^{3+} ion might be populated. Considering the small excitation cross-section of Tb^{3+} ion due to parity forbidden of intra-4f shell transitions [54] we expect that indirect excitation of Tb^{3+} ions through energy transfer from the Nb_2O_5 host matrix is probable. One can consider also involvement of energy levels above the $^5D_4$ and up to 4.67 eV (266 nm) including $^5D_{2,3}$, $^5H_{6,7}$, and $^5H_4$. Non-radiative recombinations from those upper levels may populate the $^5D_4$ level, at the origin of observed radiative transitions. However, the higher the number of recombination steps, the less efficient this mechanism is. Indeed, the probability of populating the $^5D_4$ level evolves with the product of the probabilities of each transition between the energy levels above the $^5D_4$ (*i.e.* bottleneck effect). For this reason, the $^5D_{2,3}$ levels, reported at about 3.26 eV and 3.5 eV by Dieke *et al.* [55], are most likely indirectly excited by energy transfer from some electronic states of the Nb_2O_5 host matrix. Thus, non-radiative recombinations originating from the $^5D_{2,3}$ levels can also populate the $^5D_4$ level at the origin of the radiative recombination.

Fig. 15 shows the relative PL intensity map of the main Tb^{3+} ion $^5D_4 \rightarrow {}^7F_5$ transition line as a function of T_A and Tb concentration determined by RBS. The relative PL intensity represented by the color scale framed between 0 and 1 was calculated by the ratio of integrated between 530 nm and 570 nm the $^5D_4 \rightarrow {}^7F_5$ peak intensity over the same integrated peak intensity for the sample with the most intense band. Fig. 15 shows those calculated relative PL intensity represented by the circles, the area between circles was linearly interpolated. The largest PL relative intensity is obtained with the Tb^{3+} content of 5.03 at.% and T_A = 900 °C. Fig. 15 shows two trends, first the PL emission increases and becomes measurable for an annealing temperature T_A above a threshold value, and second, the PL relative intensity increases with the Tb concentration up to a maximum and then decreases weakly. The first trend can evidence the effect of the annealing on rare-earth ions doped host matrix [54]. Thus, one may expect that Tb doping contributes to the improvement of the host matrix by traps passivation (e.i. dangling bonds at grains interface, non-radiative defects, etc) that could lead to PL quenching[53]. Moreover, we have shown in *Section 3.1* that Nb_2O_5 undergoes a structural evolution with the T_A manifested by the optical properties modification. More specifically, the observed bandgap energy shows a decrease with the T_A leading to the lowest bandgap energy values of 3.1 eV − 3.3 eV for 800 °C and 2.6 eV − 2.9 eV for 900 °C, respectively. This Nb_2O_5 bandgap energy reduction leads to a greater

Table A3
Indexing of annealed Nb_2O_5 NT0RTA800, NT1.42RTA800, NT2.42RTA800, NT3.54RTA800, NT4.67RTA800, NT4.85RTA800, and NT5.03RTA800for XRD measurements with JCPDS reference used for phase identification for TT-Nb_2O_5 and T-Nb_2O_5.

2θ							JCPDS files no.: 00–030-0873 T-Nb_2O_5 orthorhombic		
NT0A800	NT1.42A800	NT2.42A800	NT3.56A800	NT4.67A800	NT4.85A800	NT5.03A800	2θ	d (A)	hkl
22.63	22.71	22.70	22.66	22.69	22.67	22.67	22.061	3.930	(0 0 1)
28.41	28.59	28.51	28.39	28.43	28.41	28.38	28.401	3.140	(1 8 0)
28.83	28.93	28.87	29.04	29.23	29.26	28.97	28.890	3.088	(2 0 0)
–	–	–	–	–	–	–	30.168	2.960	(8 0 4)
31.65	–	–	–	–	–	–	31.937	2.800	(1 1 5)
36.58	–	36.55	36.64	36.68	36.72	36.66	36.604	2.453	(1 8 1)
37 0.01	–	37.05	37.03	36.96	–	–	36.994	2.428	(2 0 1)
46.21	–	46.38	46.42	46.34	46.31	–	46.159	1.965	(0 0 2)
51.01	–	50.96	–	50.86	–	–	50.89	1.793	(3 8 0)
55.17	–	55.33	–	55.42	55.31	–	55.368	1.658	(2 0 2)
56.44	–	–	–	56.51	–	–	56.37	1.631	(3 8 1)

Table B1
Bandgap energy obtained from VASE measurements for all doped annealed between 400 °C and 900 °C samples, with TL2 for A900 series and TL1 for other series.

		Tb^{3+} proportion					
	Name	NT1.42	NT2.42	NT3.56	NT4.67	NT4.85	NT5.03
	A400	3.46	3.47	3.48	3.5	3.48	3.407
T_A	A500	3.46	3.5	3.54	3.54	3.54	3.549
	A600	3.36	3.44	3.52	3.54	3.56	3.551
	A700	3.292	3.378	3.369	3.401	3.413	3.401
	A800	3.17	3.27	3.27	3.28	3.26	3.284
	A900	2.814	2.806	2.734	2.590	2.509	2.925

energy adaptation of the upper energy levels of the host matrix with respect to the $^5D_{2,3}$ levels, and could therefore increase indirect excitation of the Tb^{3+} ion by energy transfer from the host matrix conduction band to higher excited states of Tb^{3+} ion. For Tb-doped Nb_2O_5 annealed at a lower T_A, higher bandgap energies ranging from 3.35 to 3.55 eV were obtained, which reduced the energy match between the host matrix energy levels and the $^5D_{2,3}$ levels and subsequently alter the energy transfer efficiency. Taking into account the small direct excitation cross-section of Tb^{3+} ion and the opposite change trends observed for the bandgap energy and the relative intensity of PL, we conclude that the mechanism of excitation of the Tb^{3+} ion probably occurs predominantly via an indirect excitation by energy transfer from excited energy levels of the Nb_2O_5 host matrix to the $^5D_{2,3}$ levels.

The second trend shows that for a given annealing temperature T_A over the threshold value the PL relative intensity increases with Tb content up to a maximum followed by saturation and a shallow decrease. As an example, at $T_A = 800$ °C, the PL relative intensity increase with Tb^{3+} concentration saturates at 4.67 at.%, and then decreases. This PL relative intensity quenching is likely due to the formation of RE aggregates triggered by high Tb concentration and well known as RE concentration quenching [56,57]. The modification of the Nb_2O_5 host matrix observed in previous sections due to high Tb concentration may also play a role in the observed PL quenching.

4. Discussion and conclusion

Thin layers of Nb_2O_5 were deposited by sputtering from a high purity Nb_2O_5 target on a silicon substrate. The deposition was followed by a rapid RTA annealing step at temperatures varying between 400 °C and 900 °C. The composition of the Nb_2O_5 samples was studied through the RBS, which led to the determination of the Nb and O contents corresponding to Nb_2O_5 within the error range. The XRD measurements show that the samples of Nb_2O_5 unannealed and annealed at 400 °C and 500 °C are amorphous while the samples annealed between 600 °C and 900 °C are crystallized with a pseudohexagonal (TT- Nb_2O_5) majority phase for RTA at 600 °C and orthorhombic (T-Nb_2O_5) phase for T_A above 700 °C. This result was confirmed by TEM analysis, which proves that the Nb_2O_5 sample annealed at 800 °C is in an orthorhombic (T-Nb_2O_5) phase. The refractive index of Nb_2O_5 samples was found of two kinds, depending on annealing conditions. For unannealed and 900 °C annealed samples, the refractive index was found with a high n value (>2.3), and the extinction coefficient k was found with a high value (up to 0.25) in the visible range (between 1 eV and 3 eV). While for samples annealed between 400 °C and 800 °C the refractive index remain with a high n value (>2.3), but the extinction coefficient k was found equal to zero in a visible range (between 1 eV and 3 eV). This last kind of Nb_2O_5 presents a refractive index which is in good accordance with those reported in the literature. For Nb_2O_5 samples annealed between 400 °C and 800 °C, a small variation of refractive index n was observed leading to the determination of Nb_2O_5 film densification with increasing T_A, which is confirmed by a film thickness decrease. Nb_2O_5 thin films doped with Tb^{3+} were successfully deposited by co-sputtering of Nb_2O_5 and Tb_4O_7 targets on a silicon substrate followed by an annealing treatment. The successful Tb doping was evidenced by RBS measurements that showed for all Nb_2O_5 samples, the stoichiometry of Nb_2O_5 was kept. The Nb and O contents seem constant with increasing T_A, and Tb dopants concentration. The RBS measurement carried out on series annealed at 800 °C led to the determination of the Tb content as a function of the power density applied to the Tb_4O_7 target during the deposition, Tb^{3+} incorporation content was found evolving linearly with power density up to 2.66 $W.cm^{-2}$ for 4.67 at.% of Tb, followed by a concentration saturation approaching to 5 at.% for higher power density PD_{Tb4O7}. XRD and TEM data show that the doped sample annealed at 800 °C (sample NT4.67A800), similarly to the undoped case, has orthorhombic majority phase (T-Nb_2O_5), TEM measurements evidence the presence of other minority phases TT-Nb_2O_5 or P-Nb_2O_5 in the form of small crystallites. Moreover, TEM analysis reveals that thin films are inhomogeneous and constituted by some grains and empty cavities. In this sample, some grains have a high Tb^{3+} proportion (18.5 at.%), and other grains have a low Tb^{3+} proportion (1.1at.%). The refractive index n was found to vary inversely proportional to the Tb^{3+} content and the thickness increased. This effect could be attributed to the observed reduction of density

occurring with Tb^{3+} incorporation and is supported by TEM observation of empty cavities. The formation of these cavities seems to be triggered by the incorporation of Tb^{3+} ions in the Nb_2O_5 host matrix followed by annealing and remains partially unexplained. Raman's analysis shows different behavior of Nb_2O_5 films depending on the phase transformation driven by the annealing temperature T_A. Amorphous films do not show a specific measurable Raman signature, while a peak at 701 cm^{-1} corresponds to transverse optical (TO) mode (doubly degenerated) related to the stretching mode of NbO_6 polyhedral is observed in the Nb_2O_5 orthorhombic phase. Tb doped film show different features regarding the Nb_2O_5 phase, the unannealed amorphous Nb_2O_5:Tb^{3+} sample shows distinct broadband at ~ 808.4 cm^{-1}, while other phases do not show a Tb related Raman signature. However, the incorporation of Tb is identified by the Nb_2O_5 Raman band (701 cm^{-1} for undoped) shift with increasing incorporation of Tb, from 702 cm^{-1} to 704 cm^{-1}. This shift could confirm the formation of grains enriched in terbium, as observed by TEM.

The PL emission results from the Tb^{3+} ions thanks to radiative recombination from $^5D_4$ to ^7F_j (j = 6, 4, 3) levels. The study of the emission of PL as a function of the T_A temperature and the Tb content has enabled us to show that, the healing of optical defects and a moderate Tb content allow obtaining the PL emission. Moreover, the PL emission results from radiative recombination originating from the excited level $^5D_4$. This $^5D_4$ level is probably populated by non-radiative recombinations from higher levels, the $^5D_{2,3}$ levels immediately above $^5D_4$ are most likely excited. Given the low direct absorption cross-sections of RE ion energy levels, an indirect excitation by resonant energy transfer from Nb_2O_5 host matrix energy levels is probable. Non-radiative recombinations may populate the $^5D_4$ level at the origin of the observed radiative recombinations. Indeed, PL signals were measured for the sample annealed at 800 °C and 900 °C, and no signal was detected for other samples annealed at lower T_A. The variation of PL intensity seems to be correlated with the bandgap variation of Nb_2O_5 related to the structural modification obtained from a particular annealing temperature T_A. The Nb_2O_5 bandgap reduction observed for annealing at 800 °C and 900 °C led to a greater energy adaptation of the energy levels of the host matrix with the $^5D_{2,3}$ levels and could therefore increase indirect excitation of the Tb^{3+} ions by energy transfer from host matrix energy levels to upper levels ($^5D_{2,3}$) of Tb^{3+} ions. The excitation mechanism of the Tb^{3+} ions probably occurs via an indirect excitation by energy transfer from excited energy levels of the Nb_2O_5 host matrix to the $^5D_{2,3}$ levels. Local variation of Tb^{3+} concentration was observed by TEM, however, it was not possible de correlate this local variation of Tb content with the variation of PL emission. Nb_2O_5 film seems to be either a transparent medium with a large bandgap with poor energy matching with upper energy levels of Tb^{3+} ions or a less transparent host matrix with a reduced bandgap with more favorable energy matching with upper energy levels of terbium ions. The study of another rare earth as a dopant of the host matrix Nb_2O_5 such as Europium could lead to a greater energy matching of the Nb_2O_5 upper energy levels and the upper energy levels of RE ions.

Bryan Horcholle: Investigation, Writing – original draft, Data curation, Validation. **Christophe Labbé:** Investigation, Writing – original draft, Data curation, Validation. **Xavier Portier:** Data curation. **Philippe Marie:** Data curation. **Cédric Frilay:** Data curation. **Weiqiang Yuan:** Data curation. **Wojciech Jadwisienczak:** Data curation. **David Ingram:** Data curation. **Clara Grygiel:** . **Julien Cardin:** Conceptualization, Methodology, Formal analysis, Investigation, Writing – original draft, Writing – review & editing.

The authors declare the following financial interests/personal relationships which may be considered as potential competing interests: Bryan Horcholle reports financial support was provided by Région Normandie RIN (REFEREE). Julien Cardin reports financial support was provided by Région Normandie RIN (REFEREE). Xavier Portier reports equipment, drugs, or supplies was provided by French National Research Agency (ANR-11-EQPX-0020). Clara Grygiel reports equipment, drugs, or supplies was provided by French National Research Agency (ANR-11-EQPX-0020).

This work was financially supported by the Normandy regional research support RIN project (RIN REFEREE). The findings achieved herein are solely the responsibility of the authors. The authors would like to thank F. Lemarié for the TEM sample preparations by FIB. They also thank the "Agence Nationale de la Recherche (ANR)" in the framework of the "Investissements d'Avenir" with the reference "ANR-11-EQPX-0020" for the financial support that allowed the acquisition of the FEI FIB system (HELIOS Nanolab 660) for TEM sample preparations.

Appendix

A) XRD measurements.

Indexing of measured XRD peaks is listed in Table A1 for samples NT0A600, NT0A700, NT0A800, and NT0A900 with JCPDS reference used for phase identification. For T_A below 600 °C, no crystalline phases were measured with XRD, samples are amorphous. The crystalline phase appeared for T_A over 600 °C. XRD peaks measured on sample NT0A600 were attributed to the TT-Nb_2O_5 phase. Moreover, for samples NT0A700, NT0A800, and NT0A900, XRD peaks were attributed to the T-Nb_2O_5 phase.

Indexing of measured XRD peaks is listed in Table A3 for samples NT0A800, NT1.42A800, NT2.42A800, NT3.56A800, NT4.67A800, NT4.85A800, and NT5.03A800 with JCPDS reference used for phase identification.

B) VASE measurement.

Hereafter, bandgap energies obtained from VASE measurements for all doped samples annealed between 400 °C and 900 °C are given. For samples annealed between 400 °C and 800 °C, a Tauc-Lorentz simple oscillator TL1 model was used while for samples unannealed and annealed at 900 °C a double Tauc-Lorentz oscillator TL2 model was used.

C) Raman measurement.

The deconvoluted Raman spectra for Nb2O5 samples are shown in Fig. C.1.

References

[1] N. Hara, E. Takahashi, J.H. Yoon, K. Sugimoto, Ellipsometric Analysis of Growth Process and Corrosion Resistance of Nb2 O 5 Films Formed by MOCVD, J. Electrochem. Soc. 141 (1994) 1669.

[2] Y. Saito, T. Shiosaki, Second harmonic generation in Nb2O5 thin-film optical waveguide deposited on LiTaO3 substrate by RF magnetron sputtering, Jpn. J. Appl. Phys. 31 (1992) 3164.

[3] D. Rosenfeld, R. Sanjinés, F. Lévy, P.A. Buffat, V. Demarne, A. Grisel, Structural and morphological characterization of Nb2O5 thin films deposited by reactive sputtering, Journal of Vacuum Science & Technology A: Vacuum, Surfaces, and Films. 12 (1) (1994) 135–139.

[4] G. Agarwal, G.B. Reddy, Study of surface morphology and optical properties of Nb 2 O 5 thin films with annealing, J. Mater. Sci.: Mater. Electron. 16 (1) (2005) 21–24.

[5] N. Özer, M.D. Rubin, C.M. Lampert, Optical and electrochemical characteristics of niobium oxide films prepared by sol-gel process and magnetron sputtering A comparison, Sol. Energy Mater. Sol. Cells 40 (4) (1996) 285–296.

[6] T. Ushikubo, Recent topics of research and development of catalysis by niobium and tantalum oxides, Catal. Today 57 (3-4) (2000) 331–338.

[7] M. Fredell, K. Winchester, G. Jarvis, S. Locknar, R. Johnson, M. Keevers, Ultra-wide broadband dielectric mirrors for solar collector applications, in: F.H. Teherani, D.C. Look, D.J. Rogers (Eds.), San Francisco, California, United States, 2017: p. 101051L. https://doi.org/10.1117/12.2250632.

[8] T. Maruyama, T. Kanagawa, Electrochromic Properties of Niobium Oxide Thin Films Prepared by Chemical Vapor Deposition, J. Electrochem. Soc. 141 (10) (1994) 2868–2871.

[9] S.B. Basuvalingam, B. Macco, H.C.M. Knoops, J. Melskens, W.M.M. (Erwin) Kessels, A.A. Bol, Comparison of thermal and plasma-enhanced atomic layer deposition of niobium oxide thin films, Journal of Vacuum Science & Technology A. 36 (2018) 041503. https://doi.org/10.1116/1.5034097.

[10] K. Lazarova, M. Vasileva, G. Marinov, T. Babeva, Optical characterization of sol–gel derived Nb2O5 thin films, Opt. Laser Technol. 58 (2014) 114–118.

[11] S. Stojadinović, R. Vasilić, Orange–red photoluminescence of Nb2O5:Eu3+, Sm3+ coatings formed by plasma electrolytic oxidation of niobium, J. Alloy. Compd. 685 (2016) 881–889, https://doi.org/10.1016/j.jallcom.2016.06.192.

[12] T. Maruyama, S. Arai, Electrochromic properties of niobium oxide thin films prepared by radio-frequency magnetron sputtering method, Appl. Phys. Lett. 63 (1993) 869–870, https://doi.org/10.1063/1.109884.

[13] A.M. Al-Baradi, M.M. El-Nahass, A.M. Hassanien, A.A. Atta, M.S. Alqahtani, A. O. Aldawsari, Influence of RF sputtering power on structural and optical properties of Nb2O5 thin films, Optik. 168 (2018) 853–863.

[14] G. Deng, Terbium glows green, Nature Chem. 10 (2018) 110–110. https://doi.org/10.1038/nchem.2914.

[15] I.A. Neacsu, A.E. Stoica, B.S. Vasile, E. Andronescu, Luminescent hydroxyapatite doped with rare earth elements for biomedical applications, Nanomaterials. 9 (2019) 239.

[16] R.A. Buchanan, S.I. Finkelstein, K.A. Wickersheim, X-ray exposure reduction using RE oxysulfide intensifying screens, Radiology 105 (1972) 185–190.

[17] S.Y. Kim, Y.-H. Won, H.S. Jang, A Strategy to enhance Eu 3+ emission from LiYF 4: Eu nanophosphors and green-to-orange multicolor tunable, transparent nanophosphor-polymer composites, Sci. Rep. 5 (2015) 1–11.

[18] Y.-T. An, C. Labbé, J. Cardin, M. Morales, F. Gourbilleau, Highly efficient infrared quantum cutting in Tb3+- Yb3+ codoped silicon oxynitride for solar cell applications, Advanced, Opt. Mater. 1 (11) (2013) 855–862.

[19] C.R. Matias, E.J. Nassar, M. Verelst, L.A. Rocha, Synthesis and Characterization of Nb $_{2}$ $_{O}$ 5: L^{a} 3+, E^{u} 3+ Phosphors Obtained by the Non-Hydrolytic Sol-Gel Process, J. Braz. Chem. Soc. (2015), https://doi.org/10.5935/0103-5053.20150242.

[20] L. Petit, T. Cardinal, J.J. Videau, E. Durand, L. Canioni, M. Martines, Y. Guyot, G. Boulon, Effect of niobium oxide introduction on erbium luminescence in borophosphate glasses, Opt. Mater. 28 (2006) 172–180, https://doi.org/10.1016/j.optmat.2004.12.007.

[21] R.R. Pereira, F.T. Aquino, A. Ferrier, P. Goldner, R.R. Gonçalves, Nanostructured rare earth doped Nb2O5: structural, optical properties and their correlation with photonic applications, J. Lumin. 170 (2016) 707–717.

[22] M. Mortier, F. Auzel, RE doped transparent glass-ceramics with high cross-sections, J. Non-Cryst. Solids 256–257 (1999) 361–365, https://doi.org/10.1016/S0022-3093(99)00475-5.

[23] Ö.D. Coşkun, S. Demirela, The optical and structural properties of amorphous Nb2O5 thin films prepared by RF magnetron sputtering, Appl. Surf. Sci. 277 (2013) 35–39.

[24] Z. Meisel, C.R. Brune, S.M. Grimes, D.C. Ingram, T.N. Massey, A.V. Voinov, The Edwards Accelerator Laboratory at Ohio University, Physics Procedia 90 (2017) 448–454, https://doi.org/10.1016/j.phpro.2017.09.050.

[25] L.R. Doolittle, Algorithms for the rapid simulation of Rutherford backscattering spectra, Nucl. Instrum. Methods Phys. Res., Sect. B 9 (1985) 344–351, https://doi.org/10.1016/0168-583X(85)90762-1.

[26] J. Cardin, D. Leduc, Determination of refractive index, thickness, and the optical losses of thin films from prism-film coupling measurements, Appl. Opt. 47 (2008) 894–900.

[27] Horiba DeltaPsi2, Horiba DeltaPsi 2 software, (n.d.). https://www.horiba.com/int/products/detail/action/show/Product/deltapsi2-software-1648/.

[28] G.E. Jellison, F.A. Modine, Parameterization of the optical functions of amorphous materials in the interband region, Appl. Phys. Lett. 69 (3) (1996) 371–373.

[29] G.E. Jellison, F.A. Modine, Erratum: "'Parameterization of the optical functions of amorphous materials in the interband region"' [Appl. Phys. Lett. **69** , 371 (1996)], Appl. Phys. Lett. 69 (1996) 2137–2137. https://doi.org/10.1063/1.118155.

[30] Horiba Tauc-Lorentz, Tauc-Lorentz Dispersion Formula, (2021). https://www.horiba.com/fileadmin/uploads/Scientific/Downloads/OpticalSchool_CN/TN/ellipsometer/Tauc-Lorentz_Dispersion_Formula.pdf (accessed January 26, 2021).

[31] S. Venkataraj, R. Drese, C.h. Liesch, O. Kappertz, R. Jayavel, M. Wuttig, Temperature stability of sputtered niobium–oxide films, J. Appl. Phys. 91 (8) (2002) 4863–4871.

[32] S. Li, Q. Xu, E. Uchaker, X. Cao, G. Cao, Comparison of amorphous, pseudohexagonal and orthorhombic Nb2O5 for high-rate lithium ion insertion, CrystEngComm 18 (2016) 2532–2540, https://doi.org/10.1039/C5CE02069G.

[33] L. Frevel, H. Rinn, Powder diffraction standards for niobium pentoxide and tantalum pentoxide, Anal. Chem. 27 (1955) 1329–1330, https://doi.org/10.1021/ac60104a035.

[34] S. Tamura, K. Kato, M. Goto, Single crystals of T-Nb2O5 obtained by slow cooling method under high pressures, Zeitschrift Für Anorganische Und Allgemeine Chemie. 410 (3) (1974) 313–315.

[35] C. Nico, T. Monteiro, M.P. Graça, Niobium oxides and niobates physical properties: Review and prospects, Prog. Mater Sci. 80 (2016) 1–37.

[36] L. Gao, F. Lemarchand, M. Lequime, Exploitation of multiple incidences spectrometric measurements for thin film reverse engineering, Opt. Express. 20 (2012) 15734, https://doi.org/10.1364/OE.20.015734.

[37] L. Gao, F. Lemarchand, M. Lequime, refractive index Nb2O5, (n.d.). https://refractiveindex.info/?shelf=main&book=Nb2O5&page=Lemarchand.

[38] A.A. Atta, M.M. El-Nahass, A.M. Hassanien, K.M. Elsabawy, M.M. Abd El-Raheem, A. Alhuthali, S.E. Alomariy, M.S. Algamdi, Effect of thermal annealing on structural, optical and electrical properties of transparent Nb2O5 thin films, Materials Today, Communications. 13 (2017) 112–118.

[39] D.d.A.B. Filho, D.W. Franco, P.P.A. Filho, O.L. Alves, Niobia films: surface morphology, surface analysis, photoelectrochemical properties and crystallization process, J. Mater. Sci. 33 (10) (1998) 2607–2616.

[40] R. Brayner, F. Bozon-Verduraz, Niobium pentoxide prepared by soft chemical routes: morphology, structure, defects and quantum size effect, PCCP 5 (2003) 1457–1466.

[41] M.R.N. Soares, S. Leite, C. Nico, M. Peres, A.J.S. Fernandes, M.P.F. Graça, M. Matos, R. Monteiro, T. Monteiro, F.M. Costa, Effect of processing method on physical properties of Nb2O5, J. Eur. Ceram. Soc. 31 (4) (2011) 501–506.

[42] K.-N. Chen, C.-M. Hsu, J. Liu, Y.-C. Liou, C.-F. Yang, Investigation of antireflection Nb2O5 thin films by the sputtering method under different deposition parameters, Micromachines. 7 (2016) 151.

[43] C. Kittel, P. McEuen, P. McEuen, Introduction to solid state physics, Wiley, New York, 1996.

[44] J. Shanker, G.G. Agrawal, N. Dutt, Electronic polarizabilities and photoelastic behaviour of ionic crystals, Physica Status Solidi (b). 138 (1) (1986) 9–30.

[45] G.H. Cartledge, Studies on the periodic system. I. The ionic potential as a periodic function1, J. Am. Chem. Soc. 50 (1928) 2855–2863.

[46] J.R. Tessman, A.H. Kahn, W. Shockley, Electronic polarizabilities of ions in crystals, Phys. Rev. 92 (1953) 890.

[47] J.K. Dash, L. Chen, M.R. Topka, P.H. Dinolfo, L.H. Zhang, K. Kisslinger, T.-M. Lu, G.-C. Wang, A simple growth method for Nb $_{2}$ $_{O}$ 5 films and their optical properties, RSC Adv. 5 (2015) 36129–36139, https://doi.org/10.1039/C5RA05074J.

[48] J.M. Jehng, I.E. Wachs, Structural chemistry and Raman spectra of niobium oxides, Chem. Mater. 3 (1) (1991) 100–107.

[49] A.M. Raba-Paéz, C. Falcony-Guajardo, I. Supelano-García, M.R. Joya, Niobium pentoxide samples with addition of manganese at different concentrations and calcination temperatures applied in the photocatalytic degradation of rhodamine B, Applied Sciences. 10 (2020) 4257.

[50] D. Liu, P.E. Flewitt, Raman measurements of stress in films and coatings, Spectrosc. Prop. Inorg. Organomet. Compd. 45 (2014) 141–177.

[51] S. Schipporeit, D. Mergel, Spectral decomposition of Raman spectra of mixed-phase TiO $_{2}$ thin films on Si and silicate substrates, J. Raman Spectrosc. 49 (2018) 1217–1229, https://doi.org/10.1002/jrs.5369.

[52] S.M. Masloboeva, N.V. Sidorov, M.N. Palatnikov, L.G. Arutyunyan, P.G. Chufyrev, Niobium (V) oxide doped with Mg 2+ and Gd 3+ cations: Synthesis and structural studies, Russ. J. Inorg. Chem. 56 (2011) 1194–1198.

[53] O. Savchyn, P.G. Kik, R.M. Todi, K.R. Coffey, Effect of hydrogen passivation on luminescence-center-mediated Er excitation in Si-rich SiO 2 with and without Si nanocrystals, Physical Review B. 77 (2008), 205438.

[54] M.M. Klak, G. Zatryb, L.W. Golacki, P. Benzo, C. Labbé, J. Cardin, J. Misiewicz, F. Gourbilleau, A. Podhorodecki, Influence of rapid thermal annealing temperature on the photoluminescence of Tb ions embedded in silicon nitride films, Thin Solid Films 675 (2019) 5–10, https://doi.org/10.1016/j.tsf.2019.02.018.

[55] G.H. Dieke, H.M. Crosswhite, The Spectra of the Doubly and Triply Ionized Rare Earths, Appl. Opt. 2 (1963) 675, https://doi.org/10.1364/AO.2.000675.

[56] F. Auzel, P. Goldner, Towards RE clustering control in doped glasses, Opt. Mater. 16 (2001) 93–103.

[57] C. Labbe, Y.-T. An, G. Zatryb, X. Portier, A. Podhorodecki, P. Marie, C. Frilay, J. Cardin, F. Gourbilleau, Structural and emission properties of Tb3+-doped nitrogen-rich silicon oxynitride films, Nanotechnology. 28 (2017), 115710.